GROWTH AND USE OF CARBON NANOTUBE NANOFORESTS AS GAS DIFFUSION LAYERS IN INDUSTRIAL-SCALE PROTON EXCHANGE MEMBRANE FUEL CELLS

A THESIS SUBMITTED TO THE GRADUATE DIVISION OF THE
UNIVERSITY OF HAWAI‘I AT MĀNOA IN PARTIAL FULFILLMENT
OF THE REQUIREMENTS FOR THE DEGREE OF

MASTER OF SCIENCE

IN

MECHANICAL ENGINEERING

MAY 2017

By

Kathryn M. Hu

Thesis Committee:

Mehrdad Ghasemi-Nejhad, Chairperson
Lloyd Hihara
Scott Miller

Keywords: nanotechnology, PEM fuel cells, carbon nanotubes, gas diffusion layer

Acknowledgements

Thank you to Dr. Mehrdad Ghasemi-Nejhad for allowing me the opportunity to conduct such exciting research in an area closely aligned with my interests in sustainability and renewable energy technologies. Your mentorship and guidance throughout this research has been invaluable. My deepest gratitude goes to Dr. Scott Miller and Dr. Lloyd Hihara for contributing greatly to my academic career and serving as committee members for this thesis. I would also like to acknowledge Tina Carvalho and Marilyn Dunlap at the Pacific Biosciences Research Center and those at the Hawaii Sustainable Energy Research Facility, most notably Jean St-Pierre and Keith Bethune of Hawaii Natural Energy Institute (HNEI), for their incredible contributions to this research – without each of you this would not have been possible. Lastly, thank you to my friends and coworkers, Brenden Minei, Caton Gabrick, Jackson Poscablo, Rodel Edra, Kyle Wong, Adrian DeLeon, Sterling Gascon, David Horton, and Vamshi Gudapati for their help and insights throughout various stages of this research.

Abstract

Proton exchange membrane fuel cells are promising sources of electrical energy for stationary generation, transportation, portable and backup power. The performance is greatly impacted by a variety of factors including cell temperature, gas flow rates, reactant humidification, and water management. Water management is especially challenging involving a fine balance between adequate humidification for conductivity and flooding due to excess water. Gas diffusion layers are a component within the fuel cell designed for the functions of permeability, electrical conductivity, mechanical strength, and water management. For this research, the production and use of carbon nanotube nanoforests for gas diffusion layers was investigated due to the carbon nanotubes' inherent high electrical conductivity, permeability, and hydrophobicity. The nanoforest was used independently and paired with carbon paper and ceramic substrates. Although none of the developed diffusion layers performed better than the baseline, unexpected behaviors were observed and the path for future research is better defined.

Table of Contents

List of Tables

List of Figures

List of Abbreviations and/or Symbols

ANOVA	Analysis of variance
CNN	Carbon nanotube nanoforest
CNT	Carbon nanotube
CP	Carbon paper
CVD	Chemical vapor deposition
ECSAa	Cyclic Voltammetry Scan for Anode Electrochemical Surface Area
ESCAc	Cyclic Voltammetry Scan for Cathode Electrochemical Surface Area
GDL	Gas diffusion layer
HiSERF	Hawaii Sustainable Energy Research Facility
HNEI	Hawaii Natural Energy Institute
ICP-MS	Inductively coupled plasma mass spectrometry
ICP-OES	Inductively coupled plasma optical emission spectrometry
MEA	Membrane electrode assembly
MPL	Microporous layer
MWCNT	Multi-walled carbon nanotube
PBRC	Pacific Biosciences Research Center
PEMFC	Proton exchange membrane fuel cell (also known as polymer electrolyte fuel cell)
PTFE	Polytetrafluoroethylene
RH	Relative humidity
SEM	Scanning electron microscope/microscopy
SEM	Scanning electron microscope/microscopy
SiC	Silicon carbide
SiO_2	Silicon dioxide
SPLM	Standard liters per minute
SWCNT	Single-walled carbon nanotube
TEM	Transmission electron microscope/microscopy

Chapter 1: Introduction

Proton exchange membrane fuel cells (PEMFCs) are attractive, competitive candidates for power production and conversion devices for stationary, automotive, and portable devices compared to various other types of fuel cells. Despite technology's current trend of decreasing size, large cells represent the biggest potential market for fuel cells [1, 2]. PEMFCs in particular are touted for their high power densities, environmental benefits via low or zero emissions, and relatively low operating temperatures [3-5]. However, at the low temperatures both liquid and vapor water coexist during the cell's operation, thus creating the need for a specific water balance to maintain both high proton conduction and gas diffusion [6].

Gas diffusion layers (GDLs), a component within the fuel cell's membrane electrode assembly (MEA), have been developed to manage water and promote gas distribution to active catalyst regions in order to obtain high power densities at all current density regions. The main purpose of a GDL is the distribution of reactants to the electrode, water management, and enhanced electrical contact between the electrode and bipolar plates. For the past decade, microporous layers (MPL) of carbon papers and carbon cloth substrates and polytetrafluoroethylene (PTFE) based coatings have been the major choice for GDLs on the market [3, 4, 6-8]. However, the development of carbon nanotubes (CNT) and popularity boost of nanotechnology has opened a new area of research for materials development for PEMFC GDLs [7].

Multi-walled carbon nanotubes (MWCNT), used in this research, are coaxial groups of single-walled tubes of varied diameters formed by rolling graphene sheets in specific

orientations. Since these tubes are on the nanometer scale, depending on the chirality MWCNTs can exhibit either metallic, semi-conducting, or a combination of both properties. Despite the structural variation, CNTs have a unique combination of stiffness, strength, and endurance whereas other fibrous materials lack one or more of these qualities [9, 10]. Given the ability to transport large currents with low resistance and high hydrophobic properties and corrosion resistance, integrating MWCNTs as GDLs could potentially decrease or eliminate the need for humidification systems.

This research focused on implementing MWCNTs as GDLs in PEMFCs in order to increase fuel cell performance in terms of stability across a range of relative humidity, increased power density, and operational efficiency. The process, from growing carbon nanotubes to the implementation in a large-scale experimental fuel cell will be discussed in this work.

Chapter 2: Literature Review

2.1 Water Management

As mentioned previously, the water management within the cell as well as the proper hydration of the GDL are both key factors in the performance of PEMFCs. Although high water vapor content in the membrane favors higher proton conductivity, extra water vapor easily condenses to liquid in the electrode and GDL. Excess liquid water severely decreases fuel cell performance by hindering gas diffusion and covering active sites of the catalyst layer [6]. In a typical cell, as shown in the diagram in Figure 1, there are multiple pathways via which water can enter the cell.

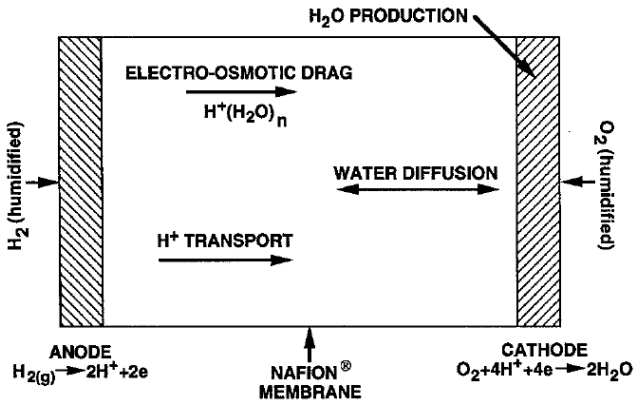

Figure 1. Modes of water transport through and uptake into a fuel cell [11].

With operating temperatures around or below 100 °C, external humidification is required to fully humidify the reactant gases in order to avoid low proton conductivity resulting from membrane dehydration. Water vapor is thereby introduced into the fuel cell via the humidified, reactant gas streams entering the electrodes. Thus, a combination of liquid and vapor water pass through each electrode to the electrode-membrane interface. The hydration of the GDL is aided

by water vapor crossing this interface. Water is also produced as the product of the oxygen reduction occurring at the cathode which is carried by electro-osmotic drag or diffusion down concentration gradients that build up within the cell. Electro-osmotic drag causes membrane dehydration when protons move from anode to cathode simultaneously transporting liquid water and water vapor [11-13].

The PEMFC's high sensitivity to hydration initiated extensive research and analysis to monitor and optimize the water management in these systems [14-17]. These studies concluded that the optimum water balance for the PEMFC model can be controlled by factors such as operating temperature, pressure, reactant gas temperatures, and the humidity of reactant gases. In addition to cell modeling, different types of PEMFC humidification systems have also been studied, including direct injection [18] which adds water directly to the gas inlets, and external membrane humidifiers [19] which flow gas over a water permeable membrane causing the gas to absorb water. One of the most common methods to combat the issue of water balance is gas bubbling which allows reactant gases to flow through bottles of heated water. The temperature of the heated water is proportional to the resulting relative humidity of the gases and can be calculated as follows in Equations (1-3) [20]. First determine the saturation pressure of water, P_w^{Sat}, at the operating temperature of the fuel cell, T_C.

$$P_w^{Sat}(T_C) = 100 \times 10^{\left[A - \frac{B}{C+T_C}\right]} \qquad \text{[kPa]} \qquad \text{(Eq. 1)}$$

$$where \begin{cases} A = Antoine\ Equation\ Constant = 4.65430 \\ B = Antoine\ Equation\ Constant = 1435.264 \\ C = Antoine\ Equation\ Constant = -64.848 \end{cases}$$

Next, determine the saturation pressure of water, $P_w^{Sat}(T_H)$, that will be required to achieve the desired relative humidity, ϕ_c.

$$P_w^{Sat}(T_H) = \phi_C \times P_w^{Sat}(T_C) \qquad \text{[kPa]} \qquad \text{(Eq. 2)}$$

Using the saturation pressure found in Equation (2), the required humidifier water temperature, T_H, can be calculated with $T°$ equal to standard temperature of 273.15 K.

$$T_H = \left[\frac{B}{A - \log\left[\frac{P_W^{Sat}(T_H)}{100}\right]} - C\right] - T° \qquad \text{[°C]} \qquad \text{(Eq. 3)}$$

2.2 GDL Composition

The material composition of GDLs also has a significant effect on the water management and conductivity within a PEMFC. The GDL, located within the MEA of a fuel cell as shown in Figure 2, is a critical component that influences the system performance especially at the high current density region as the conductive path between the bipolar plate and catalyst layer. Other functions include the passage of heat and reactant gases, mechanical support to the MEA, and protection of the catalyst layer from corrosion and/or erosion within the cell [21]. Its hydrophilicity and hydrophobicity should be balanced to simultaneously avoid flooding at high relative humidity conditions and also avoid drying at lower humidity settings in order to achieve optimum performance [4]. In order to ensure good performance, the GDL should have sufficient capabilities for gas distribution and water management, must be porous to the reactant gases, have good electrical conductivity, and be hydrophobic to prevent liquid water from saturating the material and decrease the permeability of the gas.

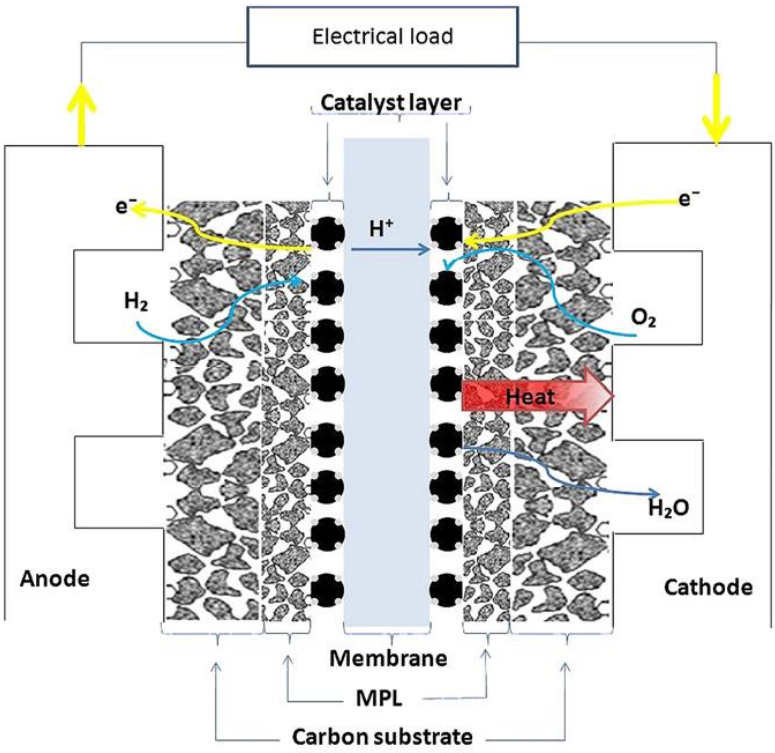

Figure 2. GDL structure and MEA components in a PEMFC with indicated electron, reactant gas, and heat flows [22].

Standard GDLs have two layers – a macroporous support layer and a microporous layer (MPL). The macroporous layer, typically a carbon fiber cloth (woven) or carbon paper (non-woven) of approximately 200-500 μm in thickness, contributes to the conductivity of the GDL [4, 23]. Extensive studies have been done to compare the performance differences of GDLs using carbon paper or carbon fiber macroporous substrates. Material characteristics, including porosity, tortuosity and surface roughness, are significant factors affecting the performance of each GDL. Figure 3 shows the structural comparisons of carbon cloth and two different carbon papers when viewed with a scanning electron microscope (SEM). For example, carbon cloth is more porous and less tortuous than carbon paper; therefore it is the better choice at high-humidity conditions. Whereas the more tortuous structure of carbon paper is more ideal for low

humidity conditions since it allows the GDL to prevent the loss of product water to dry gas streams and minimize ohmic loss [21]. However, the macro-pores often easily cause water flooding; therefore the macroporous layer is coated with a very thin, MPL of carbon black or graphite particles to increase conductivity and polytetrafluoroethylene, PTFE, to increase hydrophobicity and aid in water transport. This PTFE loading in commercial GDLs ranges from 5 wt.% to 30 wt.% and has a significant impact on the hydrophobicity and conductivity. [7, 21, 23]. The PTFE as a dielectric, however, can decrease the membrane's conductivity by blocking micropores and increasing polarization [7]. A study conducted in 2004 determined that a 10 wt.% PFTE loading on carbon cloth enabled greater output from a PEMFC, especially in the mass transfer region (> 0.8 A/cm^2) [24, 25].

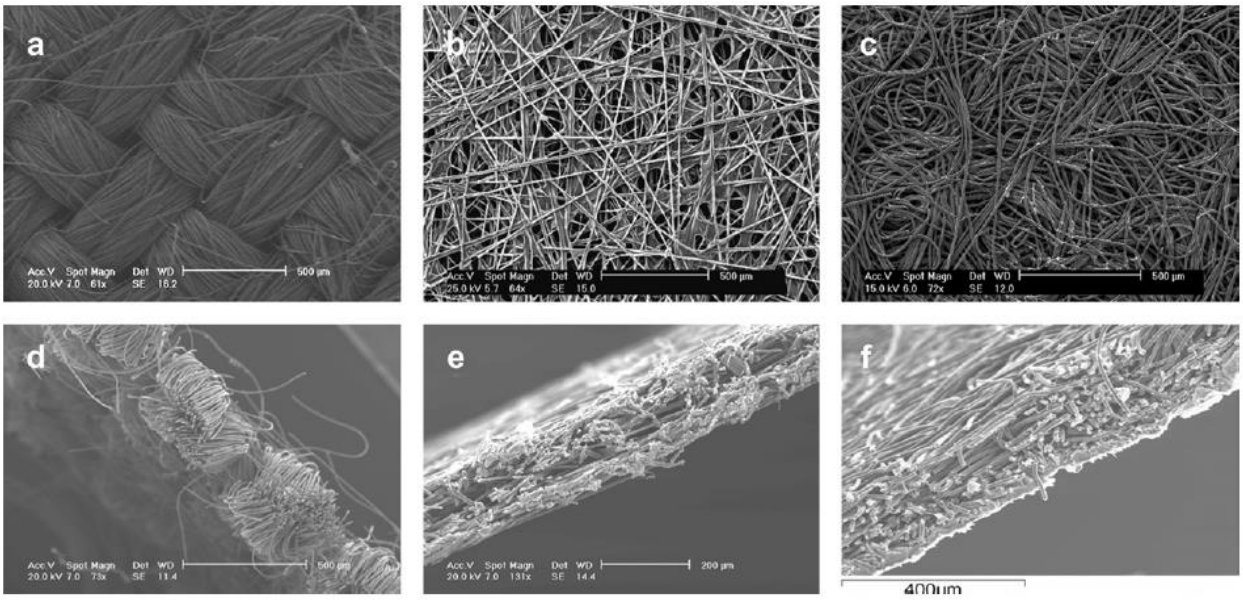

Figure 3. Scanning electron microscope images of surface and side views of carbon fiber configurations for (a) & (d) carbon cloth with woven fibers, (b) & (e) straight stretched fibers in Toray H-060 carbon paper, and (c) & (f) felt/spaghetti fibers in Freudenberg C2 carbon paper [22].

2.3 Carbon in GDLs

Other applications of carbon for fuel cells are currently being investigated aside from its use in the macroporous layer [7]. Carbon is an attractive material for electrochemical purposes; thanks to its high electrical conductivity, acceptable chemical stability, and low cost. CNTs, with an ideal combination of electrical conductivity, high surface area, and accommodating pore structure, are increasingly viewed as viable supports for catalyst materials. In 2007, Kannan *et al*. proved that nanotube can be an effective microporous layer or catalyst support material through the use of single-walled CNT (SWCNT) [3]. A mixture of 50% SWCNT and 50% Pureblack carbon with a 7 mil (approximately 178 μm) macroporous carbon paper combined with a Nafion-112 membrane electrolyte produced superior current and power densities as can be seen in Figure 4.

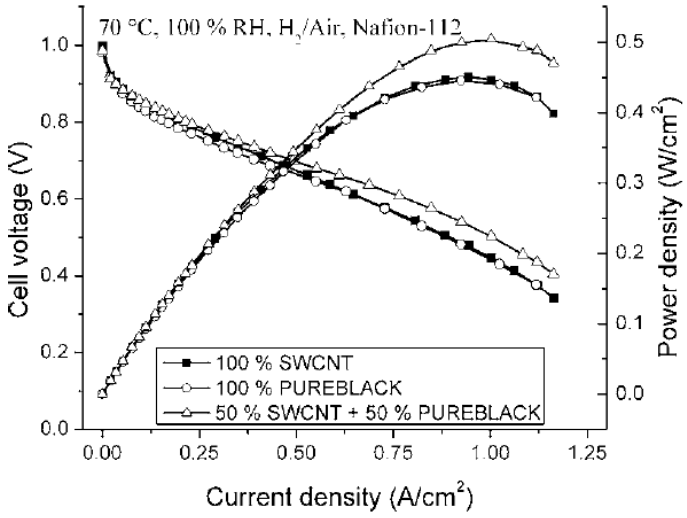

Figure 4. "Galvanostatic polarization data for MEAs at 70 °C using SWCNTs, Pureblack carbon, and Pureblack Carbon and SWCNTs (50/50 wt.%) based GDLs [3]."

These results were then further improved upon with the development of *in situ* growth of carbon nanotube nanoforests (CNN) directly onto the macroporous carbon paper layer. Using

this new GDL with the nanoforest, an array of MWCNT, on one side of the carbon paper, a stable power density of 1.100 W/cm^2 was achieved for the same operating conditions [26]. The macroporous layer used had a 15 wt.% teflonized carbon paper base. This CNN GDL exhibited stable performance at all relative humidity (RH) conditions, while the performance of wire-coated, comparison GDLs decreased drastically at lower RH levels. Figure 5 shows the improvements of the CNN GDL across a range of humidity settings in comparison to the conventional, wire-rod GDL.

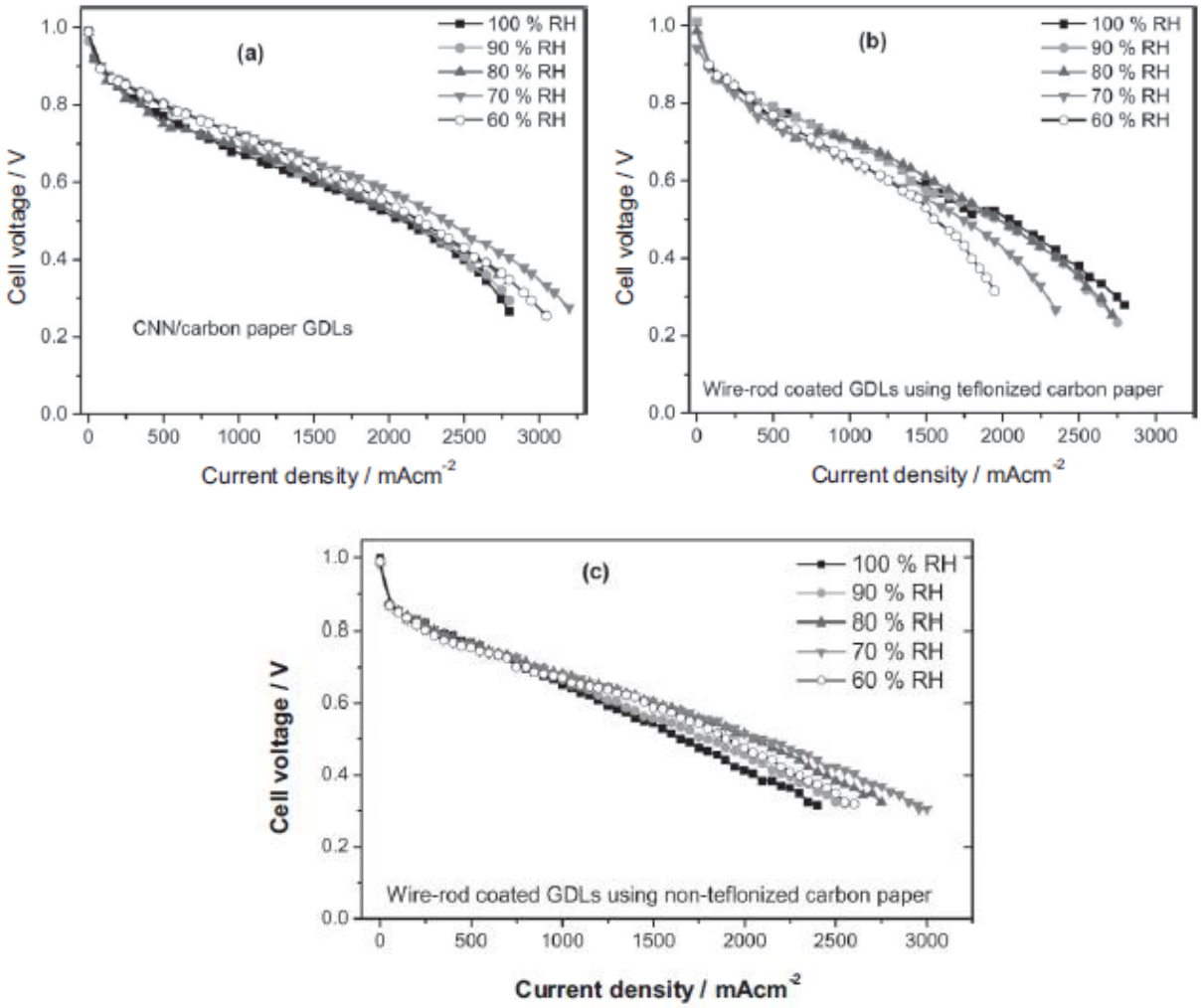

Figure 5. Fuel cell performance for GDLs based on (a) CNN/carbon paper, (b) wire-rod coating using teflonized carbon paper, and (c) wire-rod coating using non-teflonized carbon paper [26].

The following research is intended as a continuation of the above work. MWCNT CNNs are used in combination with various carbon substrates as potential, new GDL alternatives in a PEMFC.

2.4 Carbon Nanotube Growth

MWCNT can be manufactured using a number of methods, most of which consist of the nanotubes "growing" on a catalyst-coated substrate. The three most common techniques are arc discharge, laser ablation, and chemical vapor deposition. For the arc discharge method, CNTs self-assemble due to a carbon vapor created by an arc between two carbon electrodes. Arc discharge is useful when producing large CNT quantities at the expense of purity. The laser ablation option utilizes a high power laser beam on a volume of feedstock gas containing carbon (e.g. methane or carbon monoxide) and produces a small amount of pure CNTs. Chemical vapor deposition (CVD) is popular in producing MWCNT and is known as being the easiest method to scale up with the best price per unit ratio. The CVD process involves mixing a carbon-containing gas such as acetylene, ethylene, or ethanol with a metal catalyst, generally cobalt, nickel, iron, or a combination at temperature above 600 ℃ [27]. The following research utilizes a CVD furnace to grow MWCNT CNN for use as standalone GDLs or on various substrates.

Chapter 3: Methodology

3.1 CNN Growth

For this research in order to produce samples for an industrial-size fuel cell, the CNNs were grown using a six-inch diameter, Lindberg/Blue M STF55666C, CVD furnace custom-designed and fabricated at the Hawaii Nanotechnology Laboratory of the Department of Mechanical Engineering at the University of Hawai‘i at Mānoa. Substrates including silicon dioxide (SiO_2) wafers, carbon paper, and carbon ceramic cloth (further discussed in following sections) were placed one at a time upon a quartz plate at a specific location within the furnace in a predetermined optimum growth zone. Consistently obtaining good quality, uniform growth across each substrate required a significant amount of effort in order to ensure the furnace's stable operation and to determine the optimum operating parameters.

The individual and combined effects of precursor volume and precursor volumetric flow rate on the CNN growth thickness and uniform area were analyzed using a two-factor analysis of variance with three levels. Precursor temperature, furnace temperature, and gas flow rates were kept constant meanwhile the volume of precursor injected into the furnace and its volumetric flow rate were changed. The model utilized for this was as follows,

$$y_{ij} = \mu + \tau_i + \beta_i + (\tau\beta)_{ij} + \varepsilon_{ij} \qquad \text{(Eq. 4)}$$

$$\text{where } \begin{cases} i = 1,2,3 \;\; j = 1,2,3 \;\; \varepsilon_{ij} \sim N(0, \sigma^2) \\ \tau_i = \text{treatment effect of precursor volume at the i}^{\text{th}}\text{level} \\ \beta_j = \text{treatment effect of volumetric flow rate at the j}^{\text{th}}\text{level} \\ \varepsilon_{ij} = \text{error term} \end{cases}$$

A total of 18 growths with random order of testing were conducted on quartz plates as to not waste valuable, more costly substrate materials. The thickness across the plate was manually

inspected by the naked-eye and areas with noticeably thinner growth were removed. The area remaining was assumed to have uniform thickness and was measured. The CNN growth area was then scraped off from the quartz substrate and weighed. Thickness values were calculated using the measured masses and growth areas for each run.

The analysis of variance (ANOVA) tool in the Minitab17 program was employed using a general linear model with CNN growth area as the response and two factors being precursor volume and volumetric flow rate. Based on the ANOVA table generated, the flow rate was determined to be the significant factor affecting growth area. Effects analysis of the main effect plot yielded that a flow rate of 0.4 mL/min was the best option to produce the most uniform growth area of CNN.

A second general linear model was used with thickness as the response versus the same two factors. The resulting ANOVA table showed that the volume of precursor injected was the significant factor on CNN growth. Optimum values to obtain the highest thickness were determined to be 50 mL of precursor injected at 0.3 mL/min. Combining this result with that of the model for area, it was decided that the best settings to have a balance of large uniform growth area and thickness are 50 mL precursor volume and 0.3 or 0.4 mL/min volumetric flow rate. Since flow rate was not significant in determining growth thickness, 0.4 mL/min was selected for future growths as it produced the best area response and to reduce the time required. Thus, the ideal settings of 50 mL and 0.4 mL/min were used for each growth. More detailed ANOVA results can be found in Appendix A.

After placing the selected substrate on the quartz plate within the furnace, the furnace end cap was then sealed. Before each run the furnace was purged with argon gas flowing at

1.400 standard liters per minute (SLPM) while two heaters increased the front and middle of the furnace to the operating temperature of 750 ℃. Once 750 ℃ was reached and stabilized, a 1:100 by weight precursor mixture of ferrocene and xylene was vaporized at 195 ℃ in a preheater and injected into the furnace at 0.400 mL/min. Concurrently, the hydrogen gas flow of 0.300 SPLM (about 21% of the argon gas by volume) was also started which helped to carry the precursor through the furnace.

For this procedure, xylenes was the carbon-containing gas and ferrocene was the catalyst metal which produced iron nanoparticles as the base for CNT growth. As this mixture flowed into the furnace, the ferrocene particles deposited onto the surface of the selected substrate. The xylenes' carbon bonds were broken and reformed as MWCNTs on the iron nanoparticles following a base-growth model, pictured in Figure 6.

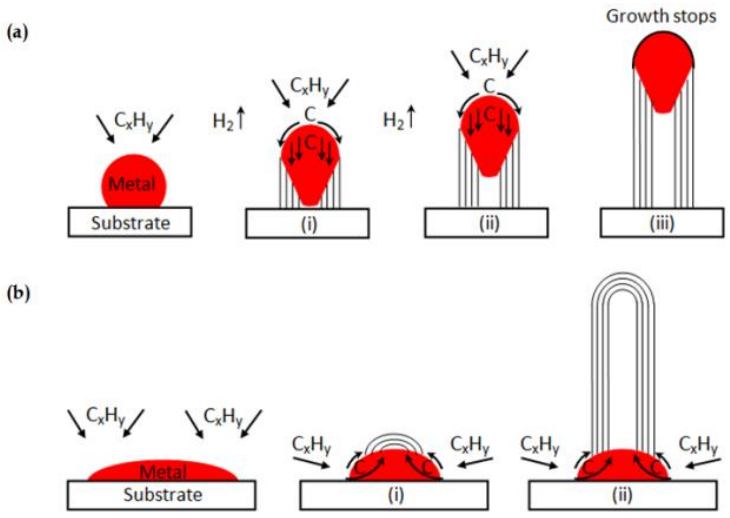

Figure 6. (a) Tip-growth and (b) Base-growth models for MWCNT CVD growth [28].

Once the entire volume of precursor was injected (requiring approximately 125 minutes), the furnace heaters and hydrogen gas flow were turned off. The CNN growth remained in an inert,

argon environment for about four hours until the furnace cooled to below 200 ℃ after which the argon gas flow was switched off.

In order to be considered for use as a GDL, each growth was visually inspected to ensure uniform growth across the substrate, an example of which can be seen in Figure 7. Uniform growth refers to the thickness such that there are no craters, pin holes, bumps, or thickness gradients as shown in Figure 8.

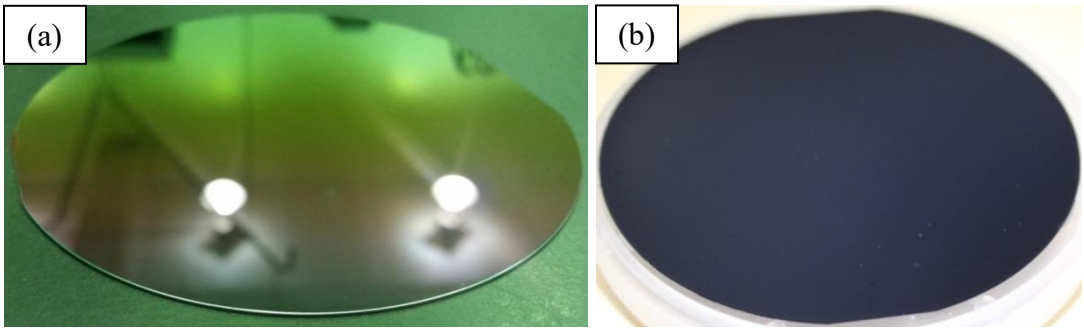

Figure 7. (a) SiO_2 wafer prior to CNN growth and (b) Ideal, uniform, good quality CNN growth from the CVD furnace.

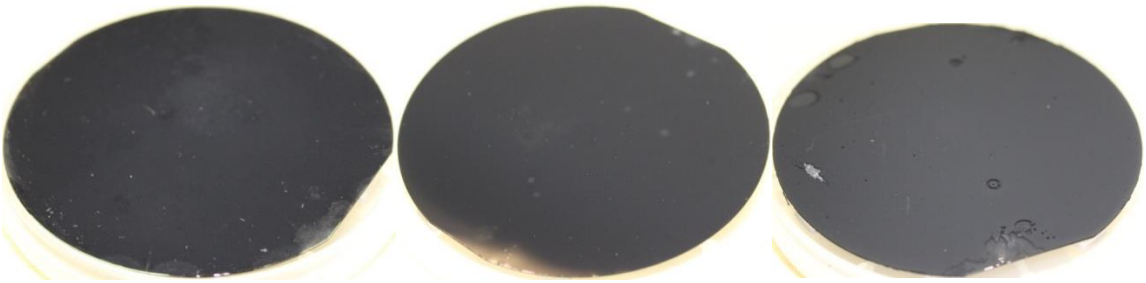

Figure 8. Examples of CNN growths with poor thickness uniformity and or pin holes.

After consistent, good quality growth could be ensured, the same parameters were used to grow CNN *in situ* on Toray TGP-H-030 carbon paper (CP) with 10 wt.% PFTE loading and eight-harness silicon carbide (SiC) Nicalon cloth. In addition to the pure CNN removed from the

SiO_2 substrate, there were four GDL variations to later be used in fuel cell testing. Each of these exhibited very different, physical characteristics that could be seen through electron microscopy.

3.2 Pure CNN Removal from SiO_2 Substrate

In order to use pure CNN as a GDL, the CNN growth needed to be removed from the SiO_2 wafer substrate it was grown on. However, since CNN are only held together by Van der Waals forces the samples were extremely fragile and difficult to handle. In prior studies, CNN was removed by dissolving the wafer's oxide layer using Sigma Aldrich Ceramic Etchant A or Alumiprep 33 [29]. Both of these chemicals are hydrofluoric acid substitutes, intended to reduce the major safety risks of working with hydrofluoric acid. In the process tested and supported by Patent #WO 2011106109 A2 "Nanotape and Nanocarpet Materials," small nanoforest samples were removed with the chemicals, then rinsed multiple times alternating between hydrochloric acid and deionized water baths to remove the ferrocene catalyst layer and leave only pure CNN [29]. Despite the success of this prior research, it was extremely difficult to obtain a full sheet of CNN with adequate thickness and a large enough area for a 50 cm^2 fuel cell to be used for an industrial-size test.

During removal testing, it was found that Alumiprep 33 was much more effective at removing the CNN than Ceramic Etchant A. The time required to separate the CNN from the SiO_2 substrate was inversely proportional to the thickness of the growth, requiring five to fifteen minutes to fully detach a CNN of approximately 200 μm instead of the predicted 90 seconds when using hydrofluoric acid. Separation initiated from any exposed SiO_2 surfaces; therefore if the growth was not uniform in thickness, spots of thinner growth would result in ruptures or tears through the CNN as can be seen in Figure 9. If the removal happened unevenly, the CNN would

also curl over on itself when removed from the substrate resulting in many unusable pieces that could not be unrolled without breaking further.

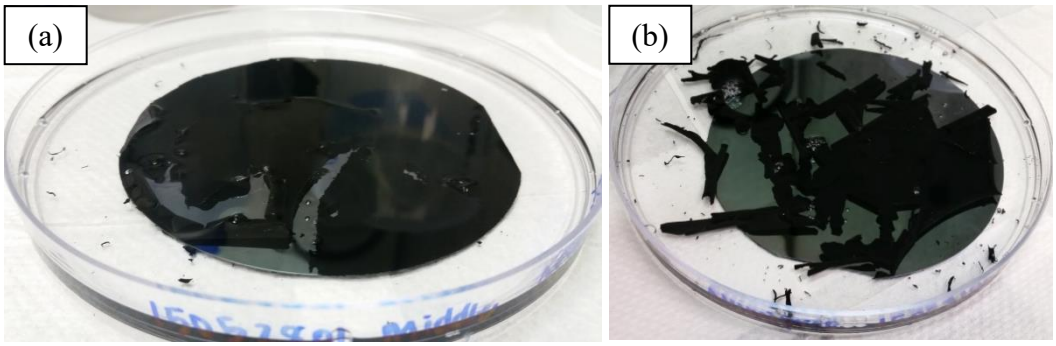

Figure 9. (a) CNN separation starting from exposed SiO_2 wafer areas and (b) Removed CNN curling on its own after lifting from the substrate using Alumiprep 33.

Further testing revealed the subsequent difficulty in handling the separated CNN pieces that would easily rip if not fully supported. Growths on the thinner end of the acceptable GDL thickness were notably more difficult to handle; therefore, thicker growths were preferred for later testing. After rinsing samples with deionized water and setting aside to dry, the pieces of growth cracked or broke into even small pieces and were then stuck to the petri dish.

In order to better control the separation process and yield complete, intact sheets of CNN the edges of the SiO_2 wafer were scraped to expose approximately 0.25 cm of wafer around the perimeter. A 10 cm x 10 cm square of 5% teflonized carbon paper was placed under the wafer to more easily lift and support the separated CNN layer after it fully detached from the substrate. The carbon paper was placed at the bottom of a square, plastic food storage container with the CNN wafer sitting on top of it. Alumiprep was poured slowly around the edges of the wafer to facilitate the edges' removal, and then the entire wafer was covered to a depth of around 1.25 cm

using 250 mL. After the CNN completely separated from the substrate, the SiO_2 wafer was carefully slid out from between the hovering CNN and carbon paper. With the CNN centered on the paper, the CNN could be fully supported as it was raised out from the Alumiprep. Keeping all of the CNN surface flat on the carbon paper, the growth was then rinsed in several consecutive baths of deionized water. The carbon paper was kept straight and inserted into the deionized water baths at nearly 90° to prevent the CNN from lifting off of the paper.

Often during the following drying period, the CNN would crack or roll off from the carbon paper likely due to any residual stresses present as well as the shrinkage differences between the two materials as they dried. Examples of these results are in Figure 10.

Figure 10. Examples of results from the drying process with the CNN on carbon paper.

To avoid this problem and keep the CNN intact, the carbon paper and CNN were soaked in deionized water for approximately two hours before drying. In addition, the drying carbon paper was supported underneath only at the edges of the CNN to eliminate possible friction with a touching surface. The paper and nanoforest were also covered to prevent forced convection which could undesirably speed the drying process. The slow drying helped the CNN to remain intact as shown in Figure 11 below. Although the developed process produced more frequent good results, not every attempt was successful.

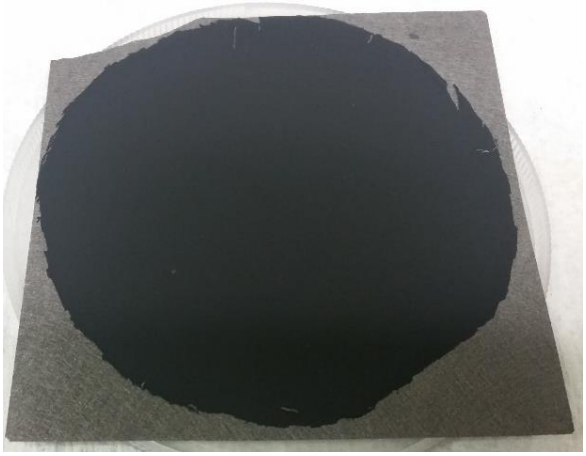

Figure 11. Complete CNN growth of approximately four inches in diameter removed from its SiO_2 substrate with Alumiprep and dried on 5% teflonized carbon paper.

Although prior research using hydrofluoric acid required the extra step of hydrochloric acid baths to remove the ferrocene, upon SEM inspection of the CNN removed with Alumiprep in Figure 12, it was determined that no defined ferrocene layer was present. A backscattering mode on the SEM also confirmed that there was no layer of ferrocene on the CNN treated with Alumiprep.

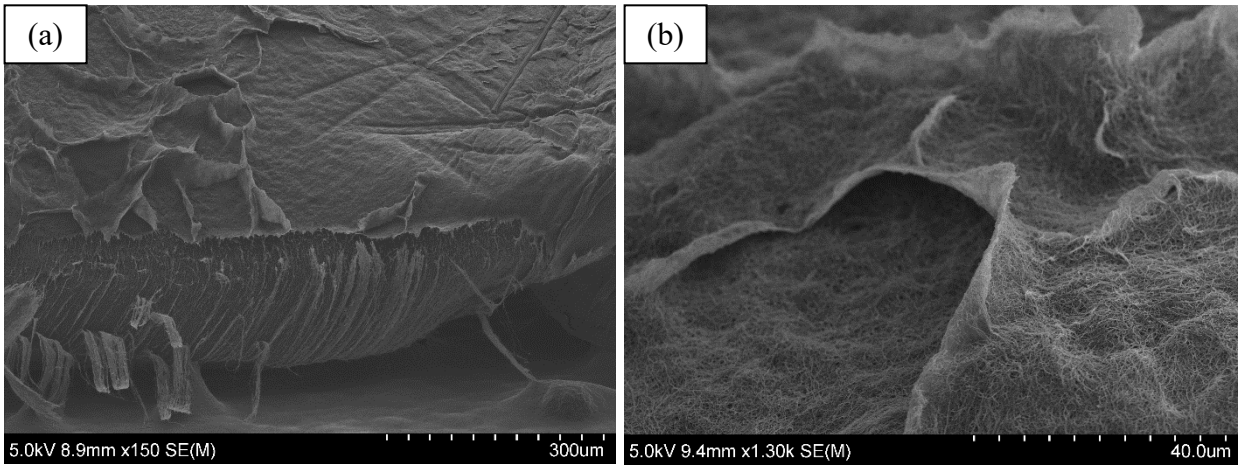

Figure 12. (a) Underside of CNN separated using Alumiprep 33 and (b) Further magnification of the surface showing what appeared to be a ferrocene layer was actually only nanotubes.

The distinction of no ferrocene layer is significant as it suggests the Alumiprep process, detailed above, not only is far less hazardous than other methods, it is also a one-step removal method rather than the previously used technique requiring further processes that could increase the potential for CNN damage.

Despite successfully producing several viable GDLs for testing, a very brief test in the fuel cell set off alarms for contamination. After verifying through assessing process purities of the entire process, see Appendix B, it was determined that the contaminants were likely from residual Alumiprep 33 that was not rinsed off. The results of a metal analysis by inductively coupled plasma optical emission spectrometry (ICP-OES) showed high quantities of iron, potassium, phosphor, and other elements (Appendix C). Since fuel cells are extremely sensitive to contaminants, it was decided that the Alumiprep process may be too risky to use since its chemical composition is not fully advertised and the CNN handling is not ideal. Therefore, a different method of removal was then investigated.

Initial attempts to scrape the layer off with a razor blade or plastic surface scraper resulted in crumbling or broken pieces, as seen in Figure 13. However, through further testing it was discovered that for the thicker growths around 200 μm the CNN layer would hold together more readily when being slowly separated from the substrate with a sharp knife. The CNN could almost be "peeled" from the wafer as the knife was slowly moved around the connected surfaces. Without a steady hand, though, any adjustments of the knife angle or wrong movements could tear through CNN.

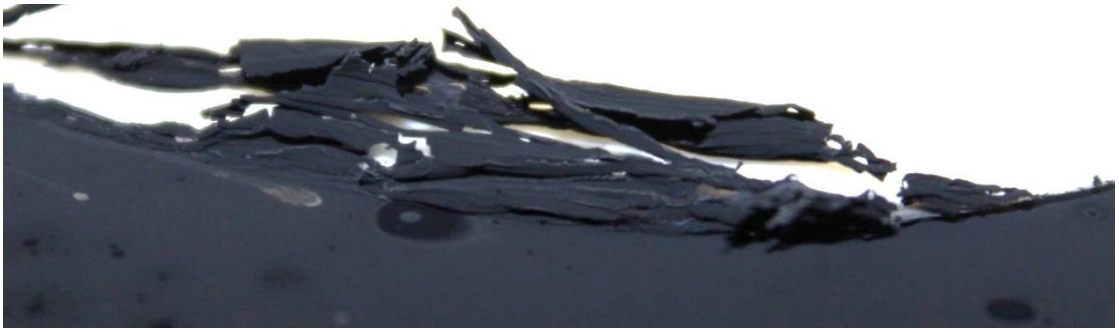

Figure 13. Broken pieces of CNN from initial attempts for mechanical removal.

Success was achieved when using an adapted wide cake lifter with an extremely sharpened edge. Since the width of the cake lifter exceeded the diameter of the wafer and CNN growth, the sharpened edge could be used to separate the CNN in one stroke. After aligning the sharpened edge with the top of the wafer, the lifter was moved smoothly across the wafer while pressing firmly downwards onto the wafer. This resulted in clean, repeatable results provided the CNN thickness was adequate and uniform, an example of which is shown in Figure 14. In order to test for contaminants again, a sample of this mechanically removed CNN was boiled in deionized water for two hours. The water was then analyzed using inductively coupled plasma mass spectrometry (ICP-MS) method and was found to have no significant metal contaminants that could leach into the fuel cell during operation (results in Appendix D).

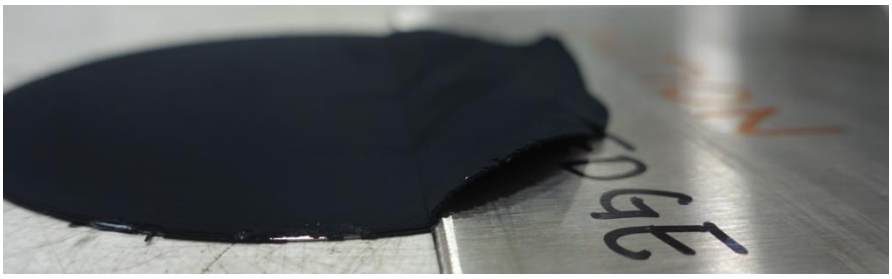

Figure 14. Removal of CNN from SiO_2 substrate with sharpened cake lifter.

3.3 GDL Characterization Using Electron Microscopy and Contact Angles

Characterization was achieved via Scanning and Transmission Electron Microscopy, SEM and TEM respectively, using microscopes at the Pacific Biosciences Research Center (PBRC) Biological Electron Microscope Facility. SEM visualization allowed for the direct observation of the MWCNT's shape, size, and structure while TEM images yielded the measurement of the MWCNT inner and outer diameters and thus the approximate number of walls [30]. Figure 15 is an SEM image of pure CNN sitting on the SiO_2 substrate. In this image it is important to note the overall verticality of the nanoforest and the thickness measurement overlaid on the image also verifying that the growth is within the appropriate range to be used as a GDL.

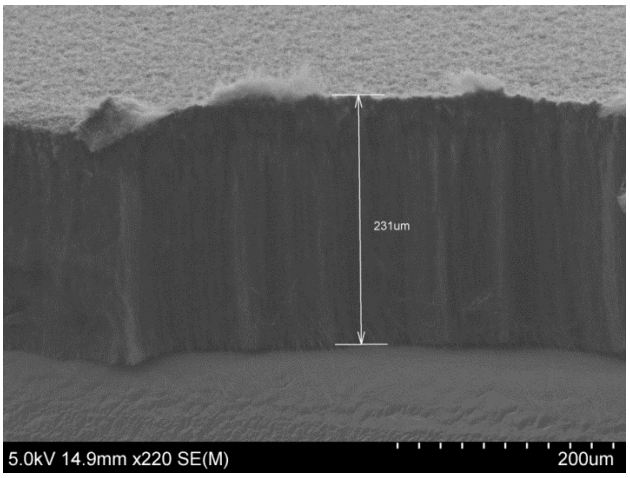

Figure 15. SEM side-view of CNN growth at 220x magnification with thickness measurement.

Figure 16 is a further magnified view of the same CNN sample which shows the actual interwoven or tangled arrangement of the nanotubes; however, the overall vertical nature is the important feature that will likely lend to better gas permeability and higher electrical conductivity along the length of the CNT [30].

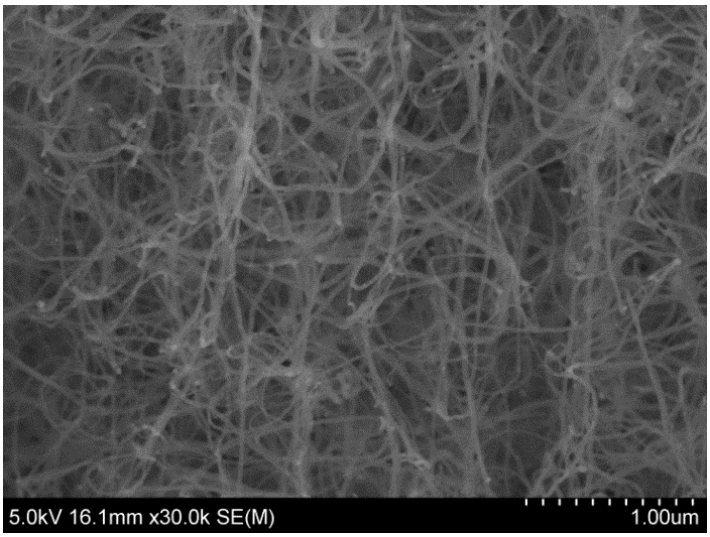

Figure 16. SEM side-view of CNN growth at 30,000x magnification.

A small amount of the nanotubes were then scraped onto a TEM film to determine the quality of the MWCNT growth through the visualization of tube walls. Distinct inner and outer walls of the CNT can be seen in the TEM image in Figure 17. From this image and similar ones, the MWCNT inner and outer diameters were measured and averaged to be 10 nm and 21 nm, respectively, or approximately 16 coaxial tubes since the distance between the concentric layers of MWCNTs is 0.34 nm [7, 27]. The darker spot within the nanotube is the ferrocene catalyst within the MWCNT.

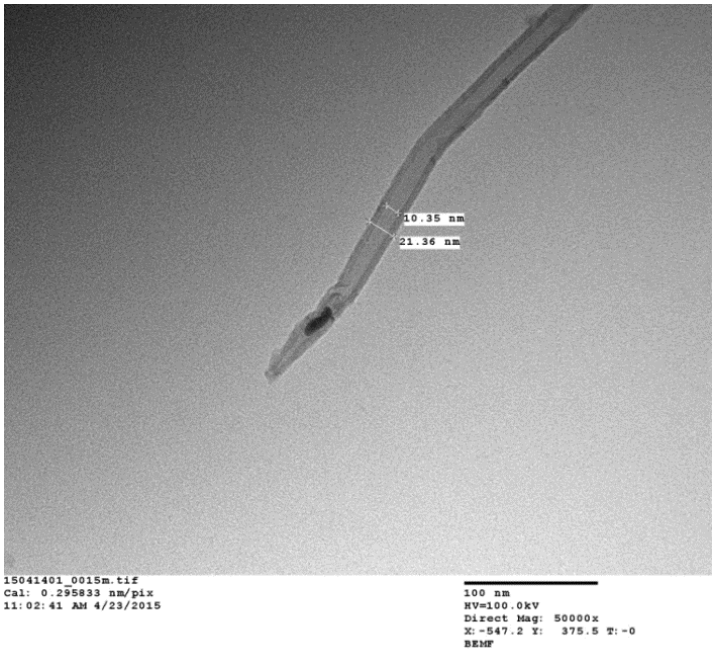

Figure 17. TEM image at 5,000x of a single MWCNT taken from the CNN.

The prior images confirmed that the designated growth parameters produced high quality, vertically aligned MWCNT as intended. Following this, each substrate and GDL candidate was analyzed using the SEM. Figures 18 through 22 show the SEM images taken for mechanically removed CNN, CP, SiC and a Sigracet baseline GDL.

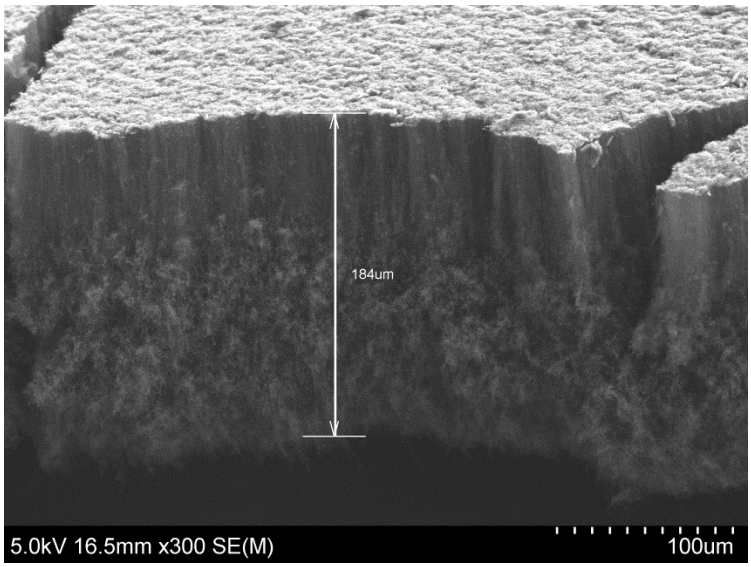

Figure 18. SEM side-view at 300x magnification of CNN growth mechanically removed from the SiO_2 wafer substrate, with thickness measurement.

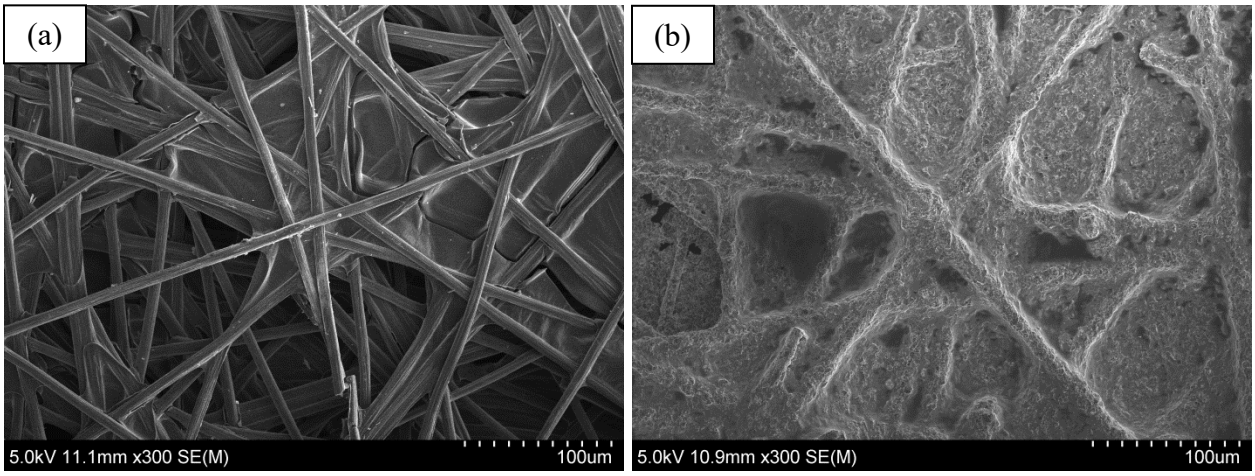

Figure 19. SEM images taken at 300x of (a) CP with 5% PTFE loading versus (b) CP with 15% PTFE loading.

In Figure 19 above, it is interesting to note the drastic difference in appearance of the CP with 5% PTFE on the left versus the 15% PTFE CP on the right. Although the PTFE distribution is not uniform throughout the paper's thickness, with more on the surfaces near the interfaces and less in the interior, from the images it is easy to understand how the PTFE content on a GDL

may affect its porosity or gas diffusion capability. Therefore the CP used as a GDL candidate was one with no more than the recommended 10% loading.

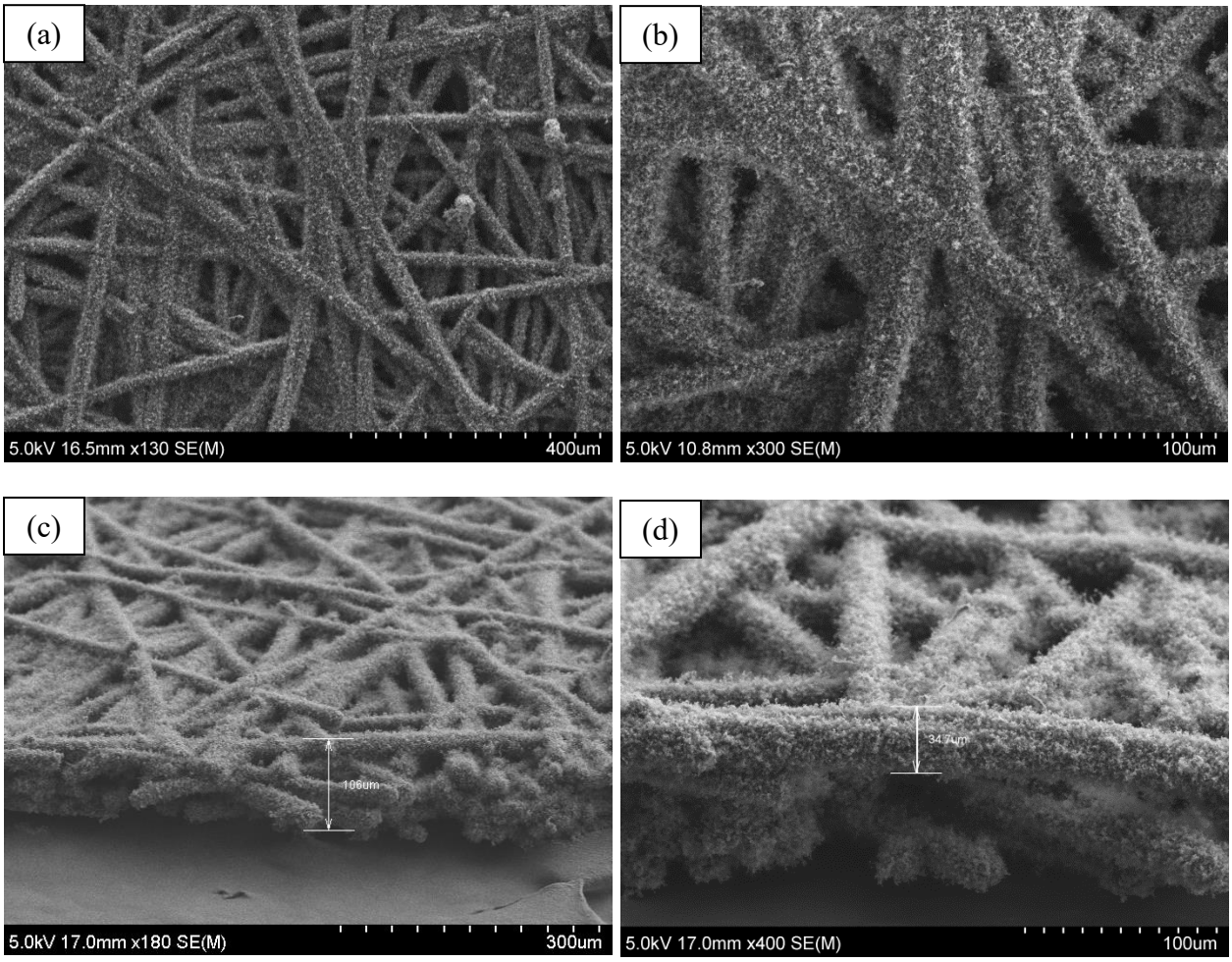

Figure 20. CNN grown in situ on CP (a) Top-view at 130x magnification, (b) Top-view at 300x magnification, (c) Side-view at 180x magnification with approximate thickness measurement, and (d) Side-view at 400x magnification with measurement of one carbon strand.

Figure 20 shows CNN growth on Toray TGP-H-030 carbon paper with 10 wt.% PTFE loading. It is interesting to note that the CNN grew uniformly on most of the exposed surfaces of the individual carbon fibers, giving an overall "fuzzy" appearance.

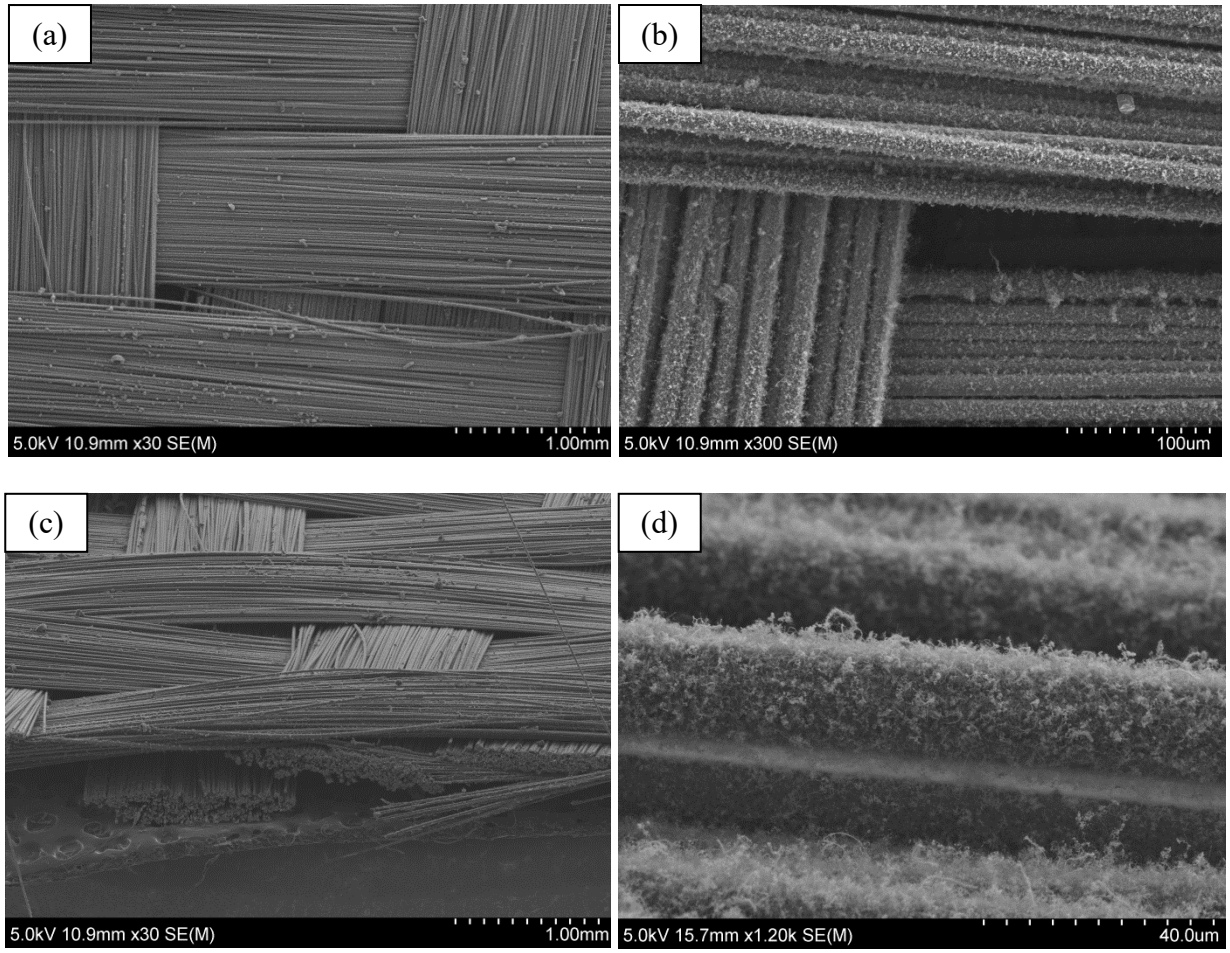

Figure 21. CNN grown in situ on SiC (a) Top-view at 30x magnification, (b) Top-View at 300x magnification, (c) Side-view at 30x magnification, and (d) Side-view at 1,200x magnification.

Since the sizing on the Nicalon was removed during the CVD furnace's heating process, the CNN was able to grow on the SiC substrate, pictured in Figure 21. Similar to the results on CP, the *in situ* growth on SiC produced strands coated in CNN, albeit a slightly thinner layer. What appears to be chunks or dust spots in Figure 21(a) are actually clusters of CNTs.

Images were also taken of a common, off-the-shelf SGL Carbon Sigracet SGL29BC GDL that was later used as a baseline reference in Figure 22. No CNN was added to this GDL. Sigracet 29 BC is a non-woven carbon paper with microporous layer on one side treated with 5

wt.% PTFE. Although it was designed for improved homogeneity and improved surface flatness [31], it is interesting to note the appearance of the mixed composition of the GDL and overall roughness of the top surface and edges. At 25,000 times magnification, the microporous carbon particles can be seen as well as the PTFE where the brighter, white spots are.

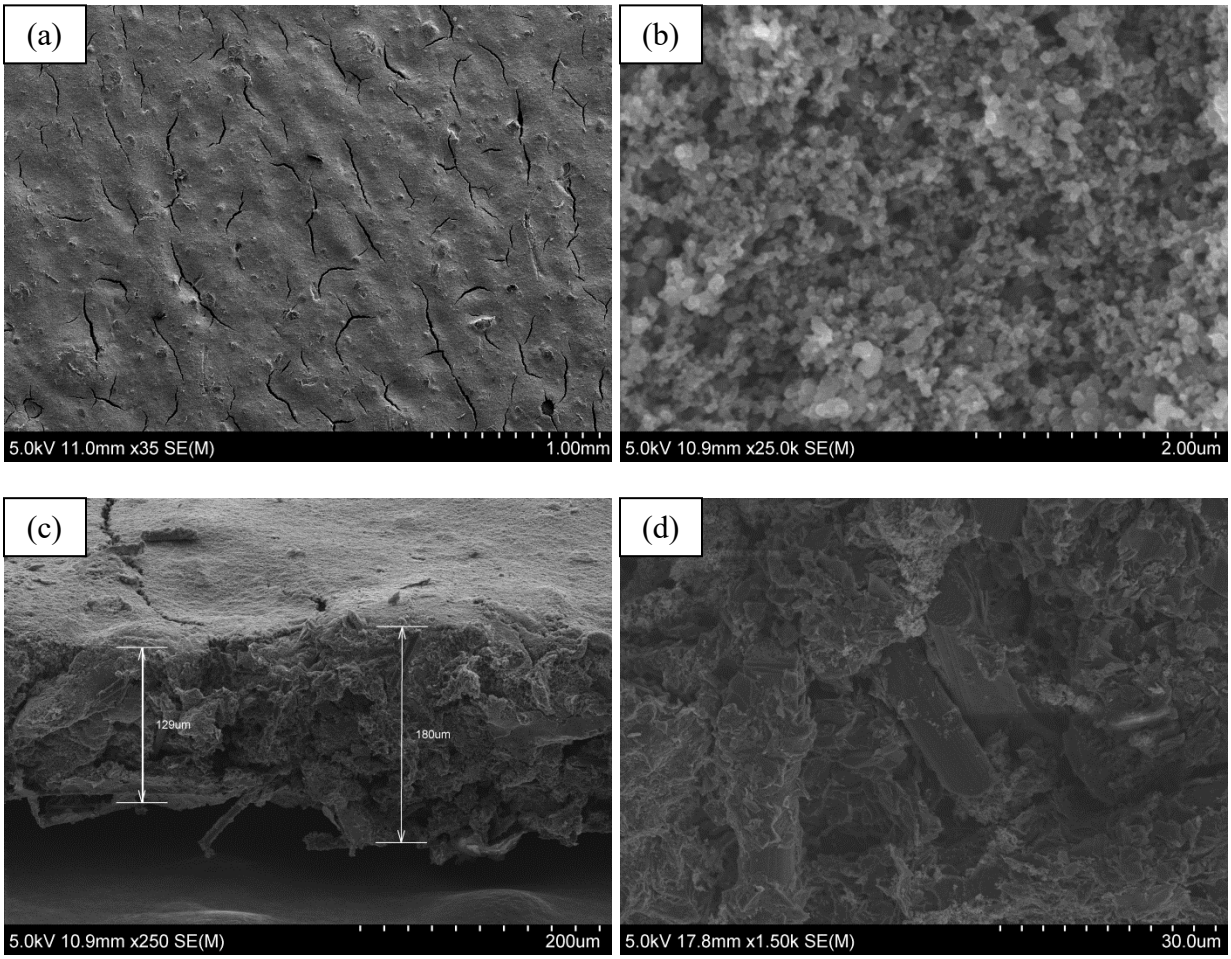

Figure 22. SEM images of the baseline Sigracet 29 BC GDL (a) Top-view at 35x magnification showing cracks on the surface, (b) Top-view at 25,000x magnification, (c) Side-view at 250x magnification with measurements, and (d) Side-view at 1,500x magnification.

In addition to utilizing electron microscopy, sessile drop contact angle measurements were taken for each GDL to be used as a rough comparison of the relative hydrophobicity or partial non-wetting behavior. Specific surface energy was not calculated as Young's contact

angle was not measured. However, the pictures in Figure 23 and associated measurements in Table 1, provided an idea of how each GDL may behave. For each substrate, a deionized water droplet of 10 μL, controlled with a 10 μL micropipette, was placed on each GDL substrate. Top and bottom contact angles were measured for the CP and SiC samples since the CNN growing process produced nanoforests primarily on the top surfaces of the substrates. Top and bottom measurements were also taken for the SGL29BC GDL. It was important to record contact angles for both sides of the GDLs as the contact angle was expected to vary through the thickness due to the amount of CNN growth and potential uneven PTFE distribution. An interesting observation for this process was the natural hydrophobicity of the CNN. When attempting to deposit deionized water droplets onto the surface, the droplet would not easily adhere to the surface or would quickly roll off. The three-phase contact angle was estimated using the ImageJ software with DropSnake plugin which fit a B-spline curve to the droplet based on manually placed knots [32]. An example of the contact angle measurement result can be seen in Figure 24.

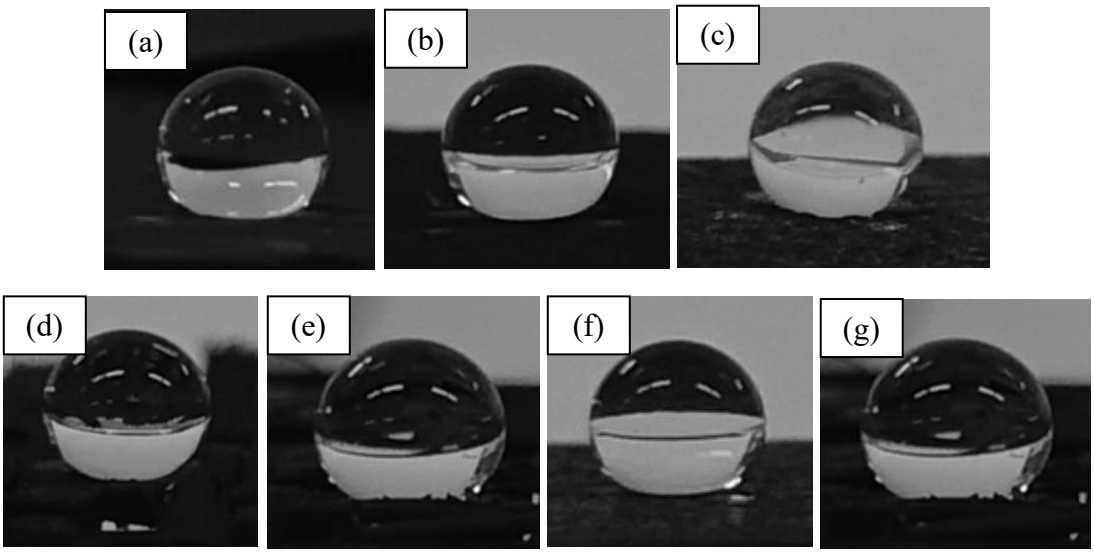

Figure 23. Deionized water droplets images for contact angle measurements on (a) pure CNN, (b) CP + CNN top, (c) CP + CNN bottom, (d) SiC + CNN top, (e) SiC +CNN bottom, (f) SGL29BC top, (g) SGL29BC bottom.

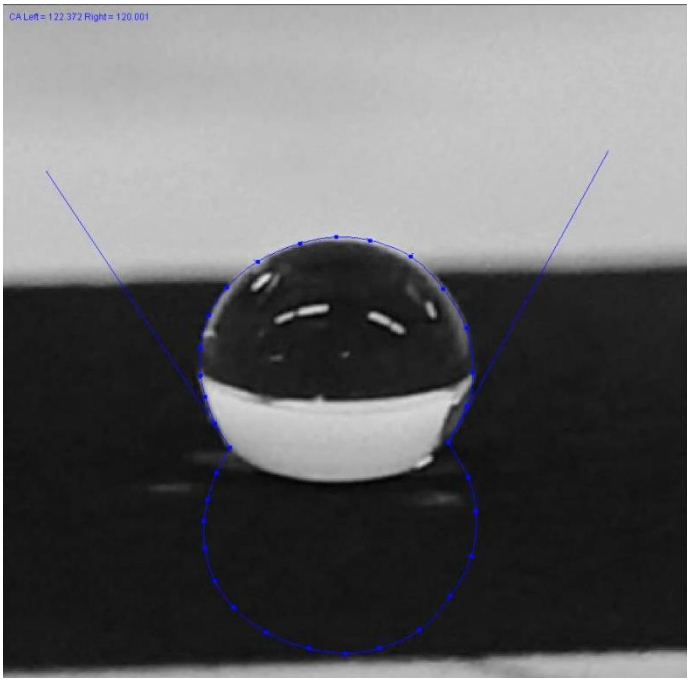

Figure 24. Example of the ImageJ DropSnake contact angle result after manually designating spline knots.

Table 1. Contact angle measurements for each GDL.

GDL Type	CNN	CP	SiC	SGL29BC
Top [degrees]	151.0	156.7	138.3	154.2
Bottom [degrees]	N/A	120.2	141.4	131.6
Average [degrees]	151.0	138.4	139.8	142.9

Since all the average contact angles in Table 1 are above 90°, none of the GDLs should be hydrophilic. Although the contact angle was not measured for the bottom of the pure CNN in this work due to its homogeneous composition, for future research it would be important to note the differences in contact angle caused by surface morphology. With the highest average contact

angle, the pure CNN GDL was expected to be the most hydrophobic – a promising outlook for its performance during fuel cell testing.

3.4 Fuel Cell Testing

For fuel cell testing, the well-established apparatus and procedures of Hawaii Sustainable Energy Research Facility (HiSERF), a branch of Hawaii Natural Energy Institute (HNEI) were utilized. Since prior research on CNN GDLs was done on a small, 1 cm^2 cell, one of the objectives of this research was to test with a larger, industrial-size cell. Therefore, a 50 cm^2 Fuel Cell Technologies cell was used. The graphite electrode plates had a triple serpentine flow field on the cathode and a double serpentine flow field on the anode, run in a counter-flow configuration. Each cell build used a GORE 5715 series MEA with 0.4 mg Pt/cm^2 loading on both sides. The MEA window frame thickness was approximately 74.3 μm and the catalyst layer thickness was around 26.8 μm. Gaskets within the cell were cut from virgin PTFE and each cell was assembled and sealed for 10% compression. The CNN GDLs were used on only the cathode side of the cell where they were expected to have the most significant impact to fuel cell performance. Each build used a different GDL. Since each GDL candidate had a different thickness, different thickness Teflon shims were employed to make sure the cell compression was consistent for each build. The measurements of all the internal cell parts are below in Table 2. The fuel cell assembly order for all the components between the anode and cathode end plates is depicted in Figure 25.

Table 2. Measurements of internal components used for fuel cell testing.

GDL Type	CNN	CP + CNN	SiC + CNN	SGL29BC
GDL Uncompressed Thickness [µm]	187	113	413	235
MEA Window Frame Thickness/2 [µm]	37	37	37	37
MEA Catalyst+Membrane Thickness/2 [µm]	13	13	13	13
Compression Percentage [%]	0.9	0.9	0.9	0.9
Compressed Thickness [µm]	168.3	101.7	371.7	211.5
Teflon Shim Thickness [µm]	145	78	348	188
Teflon Shim Thickness [mils]	5.69	3.07	13.70	7.39
Teflon Shim Thickness Rounded [mils]	6	3	14	7
Stock shims to use	6 mil	3 mil	7 mil (*2)	7 mil

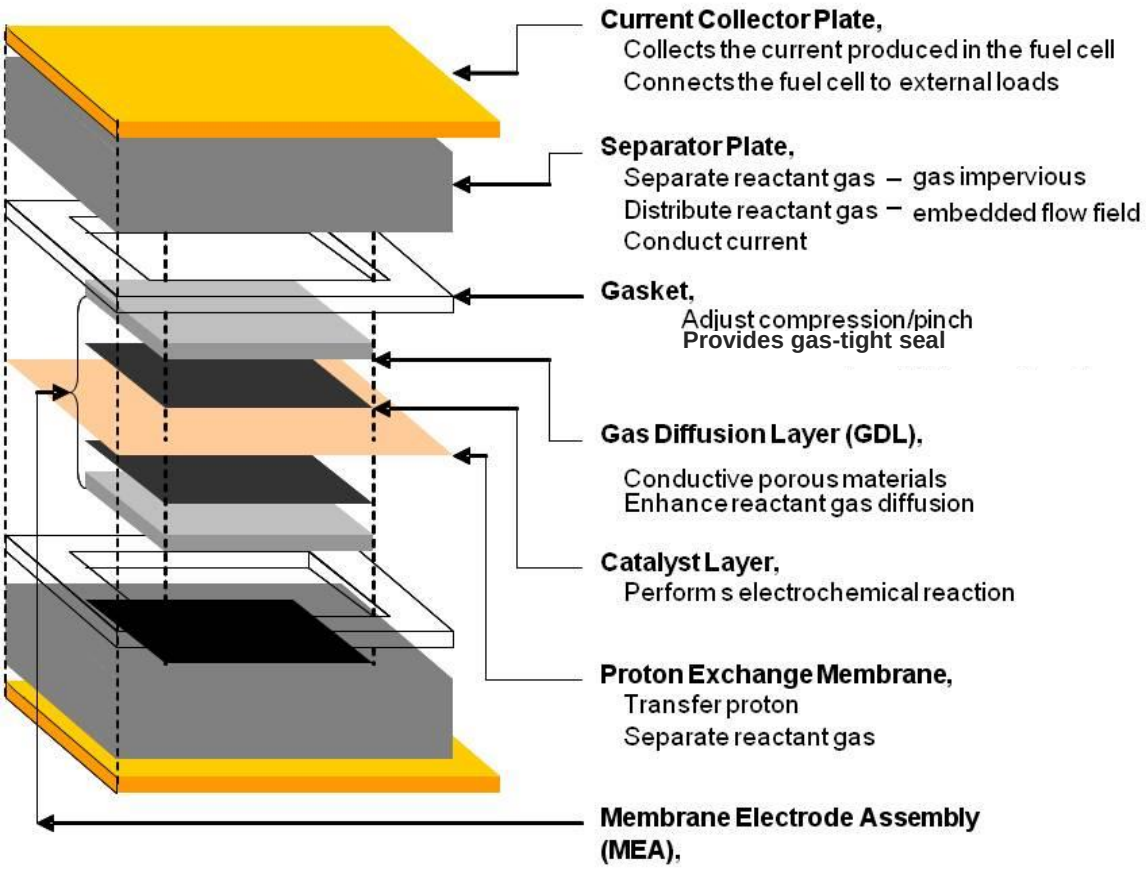

Figure 25. Diagram describing the components and their stacking order between the anode and cathode end plates [33].

For every build, the following four-day process was followed. On the first day of testing for the specific build, the MEA was first conditioned at 80 ℃ with 100% RH for both reactant gas streams and a cell pressure of 150 kPa. It underwent either 20 cycles of a Constant Voltage Step Cycle using 0.6V and 0.85 V in ten and five minute steps or an overnight constant current condition held at 50 A with 50 high/low current cycles.

On the second day the cell was cooled to 35 ℃ for MEA diagnostics. A Cyclic Voltammetry Scan for Cathode Electrochemical Surface Area (ESCAc) was conducted for three cycles where hydrogen flowed at the anode at 0.5 SLPM and a flow rate of 0.05 SLPM of

nitrogen was used at the cathode. The cell performance was scanned at a rate of 20 mV/sec and a range of 0.05 $V_{vs\ Ref}$ to 1.0 $V_{vs\ Ref}$. Next, the cell was tested for hydrogen crossover and electrical shorting. With 0.5 SLPM of hydrogen at the anode and 0.5 SPLM of nitrogen at the cathode, 0.35 $V_{vs\ Ref}$ was held for three minutes, then ramped at 5 mV/sec to 0.5 $V_{vs\ Ref}$ and held for another three minutes. Using the last five seconds of this test at each hold stop, the slope of the two point curve resulted in the shorting resistance and the short compensated current at 0.5 V is equal to the equivalent hydrogen crossover current. Finally, the Cyclic Voltammetry Scan for Anode Electrochemical Surface Area (ESCAa) was conducted with the same settings as the ESCAc, but with 0.05 SLPM of nitrogen at the anode and 0.5 SLPM of hydrogen flow at the cathode.

The third day of testing was for polarization curves taken at 70 ℃ and 150 kPa. Tests were done with hydrogen on the anode side and either air or oxygen on the cathode side with the following ratios: hydrogen/air at 2/2 stoichiometric and hydrogen/oxygen at 1.5/9.5 stoichiometric. As the cell was run through different humidity settings, 90, 70, 50, and 30 %RH, the humidity was the same on both sides of the cell. The cell was ramped up until the cell voltage read 0.3 V or the current was greater or equal to 1.75 A/cm^2 based on the maximum flow rates of the station. The High Frequency Resistance (HFR) measurements were taken at 1 kHz. Between each change of RH, an oxide cleanup routine was run with cathode reduction using hydrogen on the anode side and nitrogen on the cathode side. The fourth day repeated the procedures for gathering MEA diagnostics.

To prepare each GDL for the test cell, the material was cut with a 74.8 mm die with rounded corners an example of which can be seen in Figure 26. After assembling the stack with

a GORE 5715 series MEA with 0.4 mg Pt/cm^2 loading and designated Teflon shims, the cell was bolted together and compressed such that the final bolt torque was 40 in-lb.

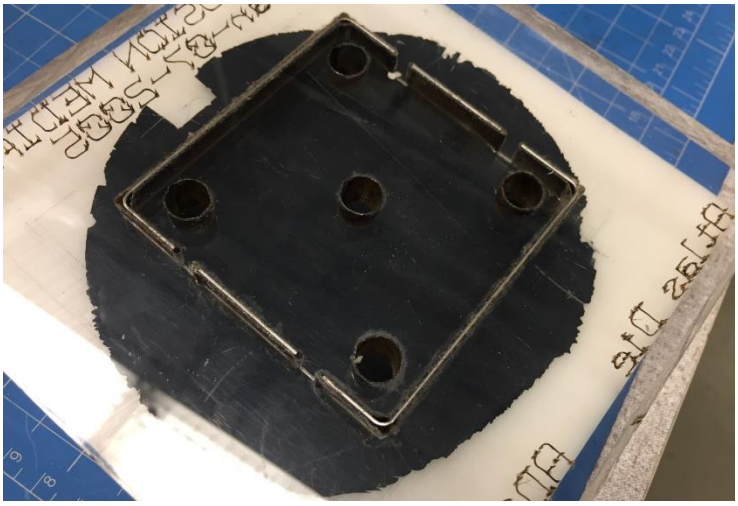

Figure 26. Original, circular CNN GDL being cut to size with a 74.8 mm die to be used as the cathode GDL.

Chapter 4: Results and Discussion

Each GDL, CNN only, CNN on CP, CNN on SiC, and the Sigracet baseline, were run through the same operating procedure as described in the Methodology section. From this procedure, polarization curves were generated for each build setup. An example of a typical polarization curve is given in Figure 27, showing the separation into three main regions. The drastic voltage drop of the top region is due to activation resistance in the oxygen reduction reaction related to the type of catalyst used. The gradual voltage drop in the second region is the ohmic voltage loss attributed to electronic, ionic, and contact resistance of the cell's components. This negative linear slope can be characterized by Equation 5 [33] in which the ohmic losses, η_{Ohm}, increase linearly with cell current.

$$\eta_{Ohm} = R_{HFR} i = (R_m + R_e) i \qquad [\Omega] \qquad \text{(Eq.5)}$$

In Equation 5, the HFR is denoted as R_{HFR} and is divided into protonic membrane resistance, R_m, and electronic resistance for the electrodes and other circuit elements, R_e. As mentioned previously, the HFR was measured during fuel cell testing.

The final sharp voltage drop in the third region is associated with mass transfer resistance, η_{MT}, described by Equation 6 [34],

$$\eta_{MT} = -\frac{RT}{n_e F} \ln\left(1 - \frac{i}{i_L}\right) \qquad [\Omega] \qquad \text{(Eq. 6)}$$

where *R* is the gas constant, *T* is operating temperature, n_e is the number of exchanged electrons, *F* is Faraday's constant, i is the current density and i_L is the current density limit. Mass transfer resistance can be especially high at the cathode of the fuel cell due to the presence of vapor and liquid water in the electrode and GDL surfaces. The presence of water vapor effectively dilutes the oxygen concentration, leading to increased mass transfer. The liquid phase water further

inhibits the transport of oxygen to the reaction cites [18]. Since no catalyst changes were made and the fuel cell testing apparatus could not reach current densities high enough for the full mass transfer range, the following results focus primarily on the cells' behavior in the ohmic region with some effects evident from mass transfer. Polarization curves for each GDL can be found in Appendix E.

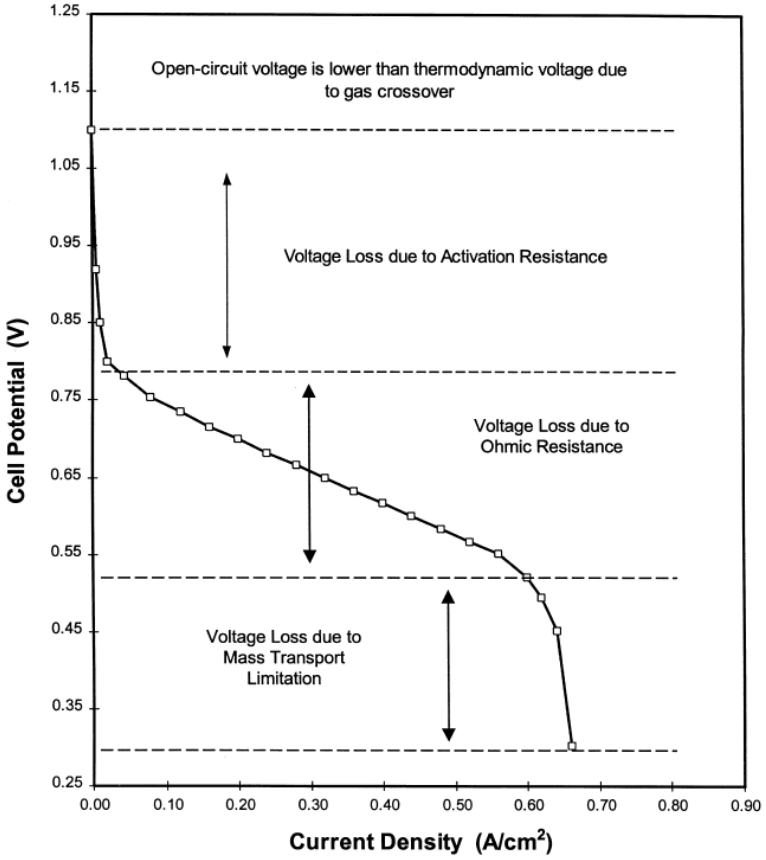

Figure 27. Typical polarization curve of a PEMFC designating three main regions: activation loss, ohmic loss, and effects of mass transfer [18].

By zooming in to the linear portion of the polarization curves, the mass transfer effects, or mass transfer resistance equivalent, can be estimated. This was done by isolating the linear portion of the curves at RH90 and RH30 for both air and oxygen. Then, a linear regression line

was fit to the data and the slopes were compared by taking the absolute value of the difference in slopes for each RH setting to provide the equivalent mass transfer resistance. An example of this can be seen in Equation 7 [35],

$$Mass\ Transfer\ Resistance\ Equivalent = \left(\left|R_{O_2} - R_{air}\right|\right)_{RH,GDL} \quad [\Omega] \quad \text{(Eq. 7)}$$

where, for a particular GDL and RH setting, R_{O_2} is the slope of the linear regression line fit to the linear portion of the data recorded from operating the cell with oxygen and R_{air} is the slope of the linear regression fit to the linear portion of data gathered from operating the cell with air. The values were calculated for RH90 and RH30 then averaged to yield a single mass transfer resistance per GDL as shown in Figure 28. Using the baseline GDL as the desired target resistance, it is clear that the CP GDL was affected the most by mass transfer when operating with air versus oxygen as its resistance is over one magnitude larger than the desired level. Although none of the CNN GDL options are below the target resistance, the SiC with CNN GDL seems to have been the least affected by mass transfer. As a continuation of this research, it will be important to further address the mass transfer effects of potential GDLs. The oxygen transport resistance can be varied by replacing nitrogen in air with helium to further separate the losses due to permeability and diffusion [34].

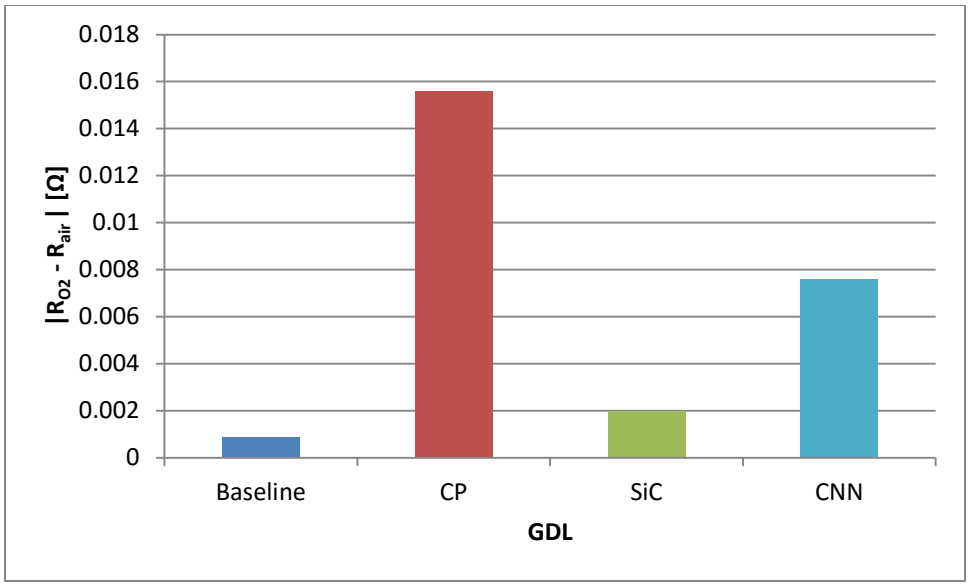

Figure 28. Comparison of equivalent mass transfer resistances for each GDL.

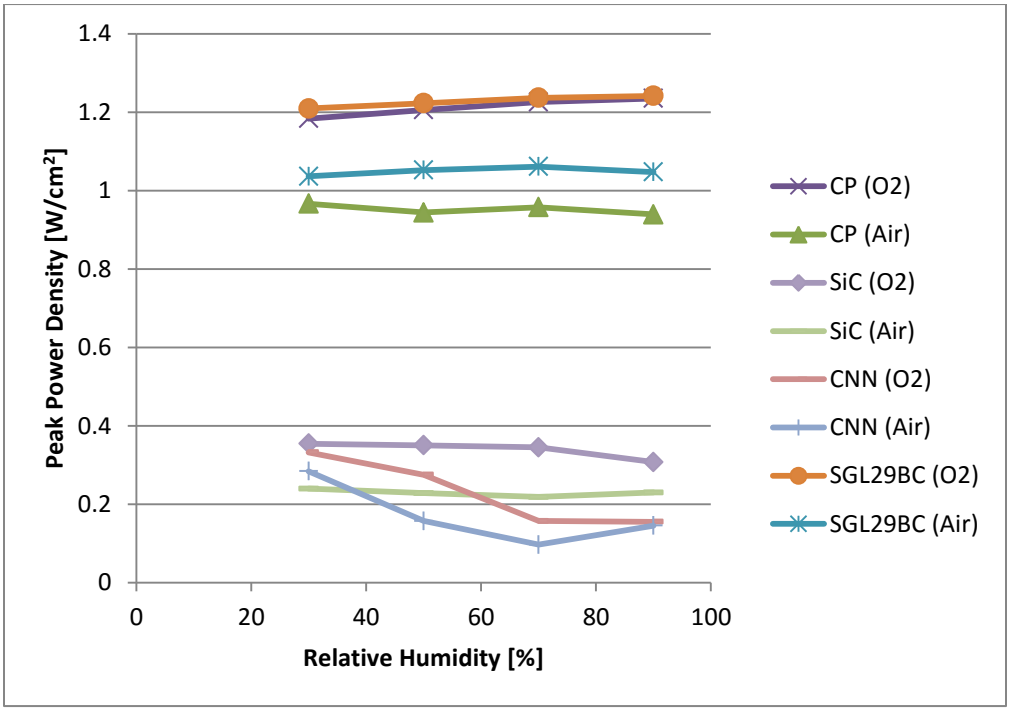

Figure 29. Comparison of peak power density for each GDL at the various RH settings.

The power density curves were constructed from the polarization curves and are given in Appendix E, from which the peak power density at various humidity levels are extracted and depicted in Figure 29. Comparing all four GDL options in Figure 29 placed the baseline SGL29BC as the top performer closely followed by the CNN on CP substrate. When operating with oxygen, the CP peak power density at each RH is nearly identical to that of the baseline GDL; however, the CP with air produced a much lower peak power density. This result is congruent with the highest mass transfer resistance shown in Figure 28. Although the polarization curves for CP look very similar to the baseline curves, the overall voltage is lower. The extra resistance in the CP GDL cannot be attributed to the CP substrate as the Toray TGP-H-030 CP through plane resistance [35] is less than that of the Sigracet SGL25BC GDL [36]. The resistance may be attributed to the presence of CNN; however it was not possible to distinguish a correlation. There was also no evidence of flooding. The SiC and pure CNN peak power densities are only approximately 28% of those for CP. This could be expected from the SiC as its resistivity before processing is two orders of magnitude larger than the SGL25BC [37]. Despite the lack of sizing and addition of CNN to increase the conductivity, it is likely not enough to offset the large resistivity. On a positive note, each of the GDLs' performance remains relatively consistent across the different RH settings, as can be seen by the nearly horizontal lines for each GDL. The pure CNN GDL was most affected by the change of RH with lower peak power density for the higher RH settings. Based on the polarization curves for the CNN GDL (Appendix E), it is evident that the best performance was obtained with the lowest RH and some amount of mass transfer was occurring even while running the test with oxygen. Therefore, it is likely that there was too much water present and liquid water

accumulated on the substrate in the form of drops or film, thereby blocking the gas transport. In addition, upon opening the cell after testing, obvious depressions from the flow channels were left on the CNN (as can be seen in Figure 30) which implies that the CNN may have been over compressed causing it to intrude into the flow fields—another potential cause for the reduced performance. Similar indentations were not present on any of the other GDLs post-testing.

Figure 30. Flow field depressions left on the pure CNN GDL during testing.

There is not enough information from these fuel cell tests to determine whether or not the addition of CNN to these substrates, or the use of CNN alone, improves or degrades the performance of the GDL (a parameter optimization is outstanding). In addition, there are many factors not considered here that can play a significant role in mass transfer. These GDL characteristics include porosity, pore size distribution, tortuosity, PTFE loading, thickness, and carbon surface state or groups. Porosity,ε, is defined as the void or pore-volume fraction of the GDL and is dependent on compressed thickness. It can be calculated using Equation 8 [38] for which d is the compressed thickness under load, d_0 is the uncompressed thickness, $\rho_{bulk,0}$ is the

bulk density of the uncompressed media, and ρ_{real} is the real density of the solid phase. Porosity can also be measured or calculated from the bulk density of the GDL based on the areal weight and thickness or the difference of weight of the sample before and after being soaked in a wetting liquid which fills all the pores.

$$\varepsilon = 1 - \left(\frac{\rho_{bulk,0}}{\rho_{real}}\right)\left(\frac{d_0}{d}\right) \quad \text{(Eq. 8)}$$

Pore size distribution is the probability density function of the distribution of pore volume by a characteristic pore size. The pore size distribution is important due to the impact on capillary pressure forcing water out of the fuel cell and is generally measured using a mercury porosimeter through which the measured permeability corresponds to the mercury permeation through the GDL with increasing pressure. Tortuosity, τ, in Equation 9 [39] is the ratio of the actual path length, L_{actual}, through pores to the shortest linear distance between two points or the material's thickness, t_{GDL}.

$$\tau = \frac{L_{actual}}{t_{GDL}} \quad \text{(Eq. 9)}$$

Porosity, pore size distribution, and tortuosity directly affect the gas and water transport through the GDL and allows for the calculation of the effective diffusion coefficient – another important parameter. Porosity and tortuosity are also both affected by PTFE content and the MPL. Generally, as can be imagined given the visual differences of the CP samples in Figure 19, PTFE loading decreases the porosity and tortuosity of the GDL by blocking potential pathways. The MPL further limits the size of the pores and their availability thereby decreasing porosity and increasing tortuosity. In addition, pore size distributions for woven carbon cloths follow a different trend than that of GDL CPs. Compression plays a significant role in these measurements as the materials are made of porous networks, rather than discrete pores. Thus the

differences in porosity, pore size distribution, and tortuosity with and without compression can impact the cell's performance. The GDLs thickness also is proportional to its through-plane resistance [22, 38, 40]. Therefore, there must be a balance between the compressed thickness and porosity, pore size distribution, and tortuosity in order to have the least resistance and highest gas and water transport capabilities. For further CNN GDL testing and analyses, these parameters should be evaluated in order to better characterize the performance of the GDLs.

Chapter 5: Conclusions

PEMFC have the great potential to be widely implemented in a range of applications from transportation to stationary power. However, water management during cell operation is still a significant challenge in the development of new cell components. CNNs are a great candidate to be used as a stand-alone GDL or with existing GDL macroporous layers due in part to its increased conductivity and natural hydrophobicity. Although none of the candidates presented in this research performed better than the current off-the-shelf GDL and only CNN on CP performed similar to it with oxygen and close to it with air, there is further room for investigation and improvements of these CNN GDLs. For future CNN GDLs research the specific contribution of the CNN should be determined by testing the macroporous layers' performance versus the GDL when the CNN growth is added *in situ*. Since flooding likely occurred during this research at higher relative humidity levels despite each GDL's proven hydrophobicity, the addition of a small amount of PTFE to the CNN and its effect would also be an interesting option to investigate. With more time, the separation of mass transfer effects into diffusion and permeability contributions should be determined by varying oxygen diffusivity during testing. Further characterization of each GDL is necessary to distinguish the significant features contributing to the fuel cell's performance.

Appendices

Appendix A: CNN Growth Parameter Effects Analysis

Experimental Design and Procedures

CNN growth will be accomplished using a chemical vapor deposition (CVD) process and furnace. In this process the precursor, a liquid solution containing iron and carbon elements, is vaporized and injected into the furnace. Within the furnace the carbon-containing gas breaks down, the iron deposits onto quartz plate substrates, and the carbon nanotubes begin forming from the iron nucleation sites. This process is highly dependent on the furnace temperatures and conditions, thus one area within the furnace has been distinguished as the best growth zone. A quartz plate placed in this zone will be the substrate for the CNN growth observed in this experiment. Precursor temperature, furnace temperature, and gas flow rates will be kept constant meanwhile the volume of precursor injected and its volumetric flow rate will be varied.

The goals of this experiment are to statistically determine,

1. The effect of the precursor volume on the growth of CNN
2. The effect of the precursor volumetric flow rate on the growth of CNN
3. The regression of the CNN uniformity and thickness based on adjustments of the precursor volume and volumetric flow rate.

The factors and levels are displayed in Table A.1 below. Two replicates will be used for each level combination.

Table A.1: Experimental Levels for Each Factor

Factor	**Levels**	
A	1	40 mL
	2	50 mL
	3	60 mL
B	1	0.3 mL/min
	2	0.4 mL/min
	3	0.5 mL/min

The order of testing was determined randomly. The number of runs conducted per day was purely based on available time since each run required approximately seven hours from start to finish. The testing order is listed in Table A.2.

Table A.2: Testing Order

Day	Volume (mL)	Flow Rate (mL/min)
1	60	0.3
2	60	0.4
3	50	0.5
	40	0.3
4	50	0.3
	40	0.4
5	60	0.5
	40	0.5
6	50	0.3
7	50	0.4
8	40	0.3
	60	0.5
9	40	0.4
	60	0.3
10	50	0.5
	60	0.4
11	50	0.4
	40	0.5

After each run, the designated plate was removed from the furnace. The thickness across the plate was manually inspected by the naked-eye and areas with noticeably thinner growth were removed. The area remaining was assumed to have uniform thickness and was measured. This growth area was then scraped off from the quartz substrate and weighed.

Results

Model and Hypothesis

The project requires a model in order to have a better knowledge of the results that will be obtained with Minitab. In this project, we considered two-factor analysis of variance with three levels. The model is then,

$$y_{ij} = \mu + \tau_i + \beta_j + (\tau\beta)_{ij} + \varepsilon_{ij} \quad (1)$$

$$i = 1,2,3 \;\; j = 1,2,3 \;\; \varepsilon_{ij} \sim N(0, \sigma^2)$$

Where

τ_i = treatment effect of Factor A at the i^{th} level.

β_j = treatment effect of Factor B at the j^{th} level.

ε_{ij} = error term.

Area Analysis

In order to achieve the goals of the project, the data was illustrated using Minitab in the form of two different boxplots. Firstly, the box plot of uniform growth area, Figure A.1, shows that the maximum of area obtained in each volume level is with a flow rate of 0.4 mL/min. However, one value should be the maximum, thus deeper analysis is required and an ANOVA table will help determine the significant factors and interactions.

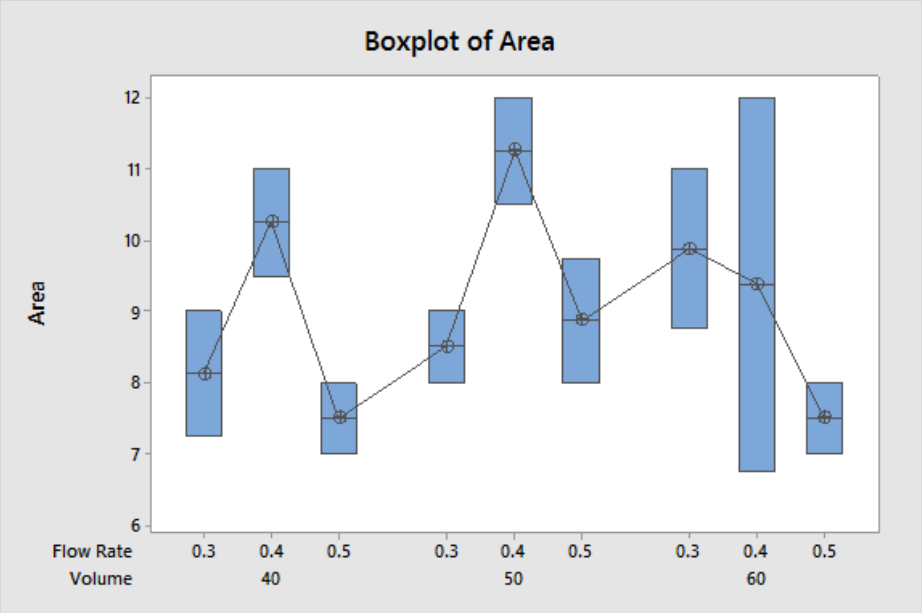

Figure A.1. Boxplot of collected CNN area measurements.

Analysis of Variance

The ANOVA analysis was conducted using a General Linear Model with Area as the response and two factors being Volume and Flow Rate. It was necessary to double check the residual plot for both responses because any outlier values would appear in the standardized

residual. Though the data appears to fit well in the Area residuals in Figure A.2, Minitab identified a total of two outliers to be removed. The resulting residual plots are in Figure A.3.

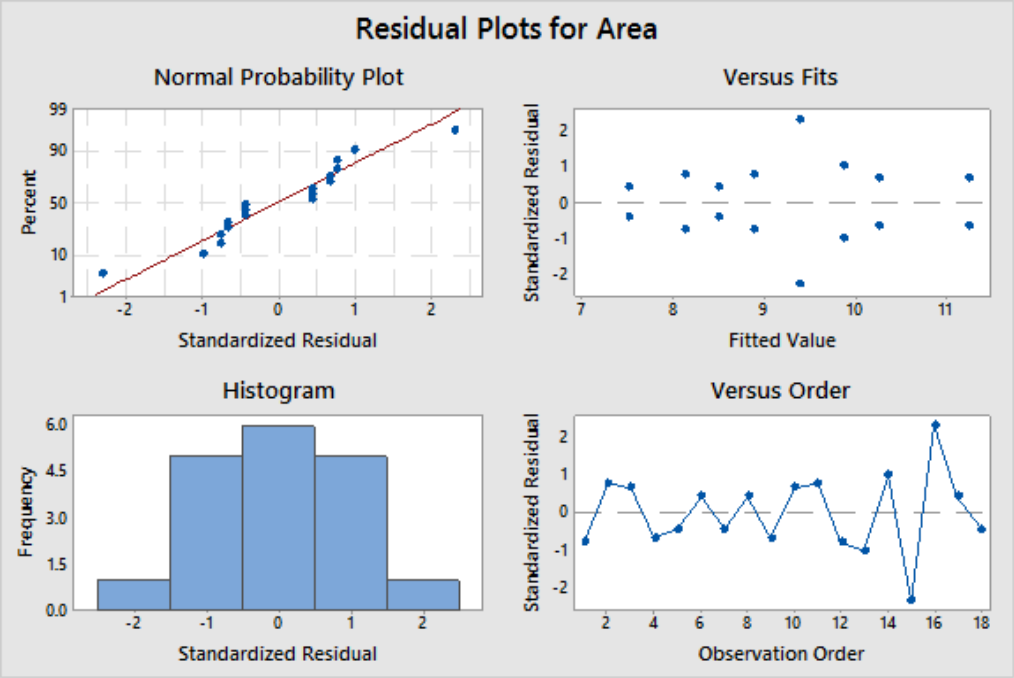

Figure A.2. Residual plots for area for the original model.

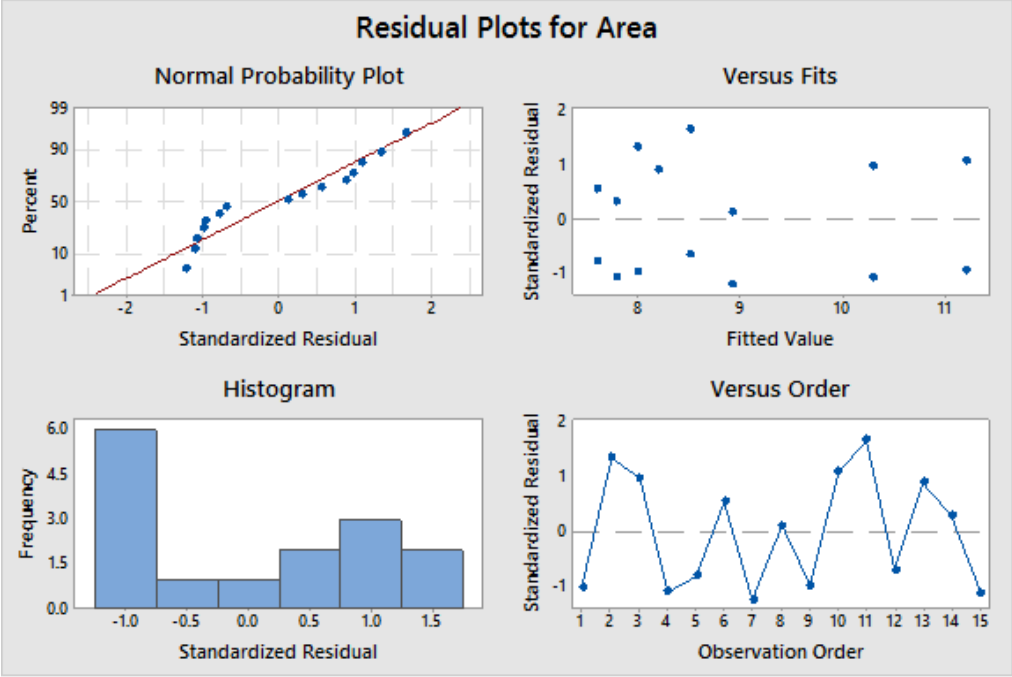

Figure A.3. Residual plots for area of the refined model after removing outliers.

The ANOVA table was then used to determine the significance of the factors. Starting with the Area response, after removing the two outliers the two-way interaction was not possible to represent. Minitab produced the error stating it cannot estimate the Volume*Flow Rate term, so this term was removed.

Analysis of Variance

Source	DF	Adj SS	Adj MS	F-Value	P-Value
Volume	2	2.671	1.3357	1.68	0.235
Flow Rate	2	17.107	8.5534	10.75	0.003
Error	10	7.956	0.7956		
Lack-of-Fit	3	1.143	0.3811	0.39	0.763
Pure Error	7	6.813	0.9732		
Total	14	30.850			

Model Summary

S	R-sq	R-sq(adj)	R-sq(pred)
0.891949	74.21%	63.90%	42.54%

Coefficients

Term	Coef	SE Coef	T-Value	P-Value	VIF
Constant	8.995	0.252	35.68	0.000	
Volume					
40	-0.370	0.328	-1.13	0.286	1.14
50	0.547	0.328	1.67	0.127	1.14
Flow Rate					
0.3	-0.630	0.328	-1.92	0.084	1.48
0.4	1.667	0.364	4.58	0.001	1.62

The ANOVA table shows that the Volume factor is not significant due to the value of p-value being higher than 0.05. The second factor, Flow Rate, is determined to be significant to the Area response because p-value is smaller than 0.05. Therefore, in the Flow Rate levels the only value which is significant is 0.4 mL/min. In this case the R^2 is 74.21%, which represents a typical experiment value.

Effects Analysis for Optimum Values

In order to determine the maximum value of our experiments main effect plot for Area is displayed in Figure A.4. It can be seen that the highest value of Area determined by Volume is achieved with 50 mL of precursor. Similarly, the main effect plot of Area determined by Flow Rate shows the highest response at 0.4 mL/min. According to the ANOVA results, Flow Rate of 0.4 mL/min is significant, so both of them have the same conclusion. The Volume factor was

not shown as significant in the ANOVA table so the 50 mL setting is chosen as the best option to have the highest Area response.

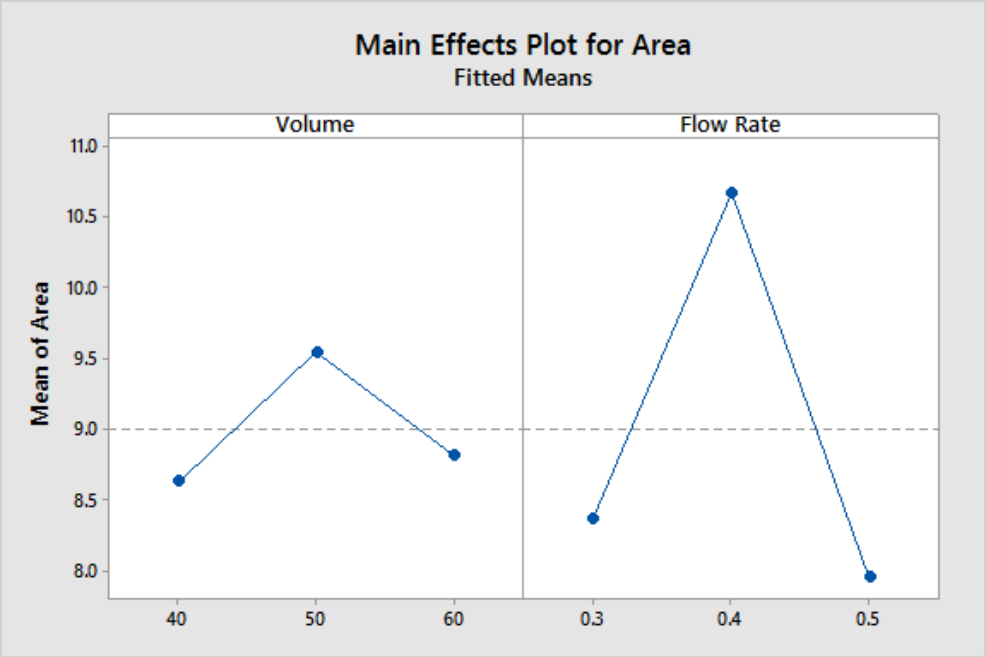

Figure A.4. Main effects plot of the uniform Area response with respect to Volume and Flow Rate factors.

Thickness Analysis

The boxplot of thickness in Figure A.5 shows that the maximum of thickness value in each volume level is also with 0.4 mL/min flow rate. The data ranges across the different factors settings make it unclear which factors produce the best thickness; thus further analysis is required.

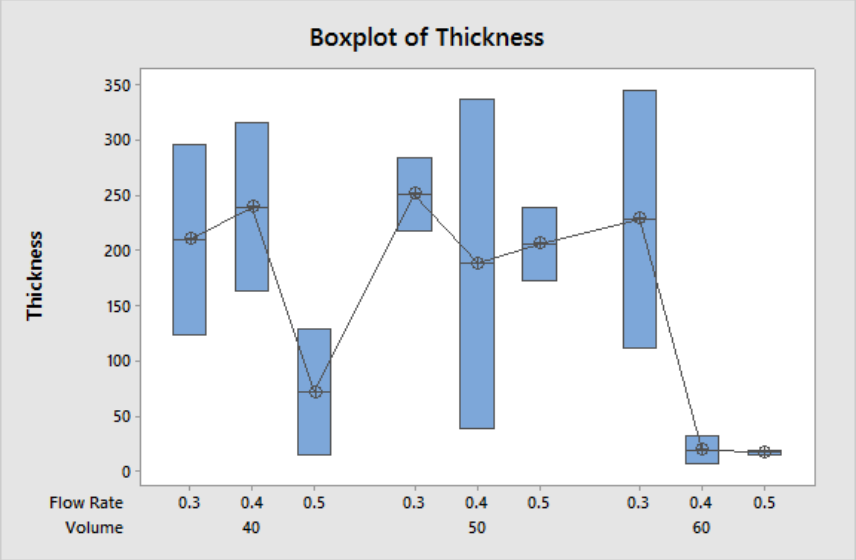

Figure A.5. Boxplot of collected thickness data.

As can be seen in Figure A.6 below, the Thickness standardized residual showed all data points very close to the line and Minitab produced no outliers.

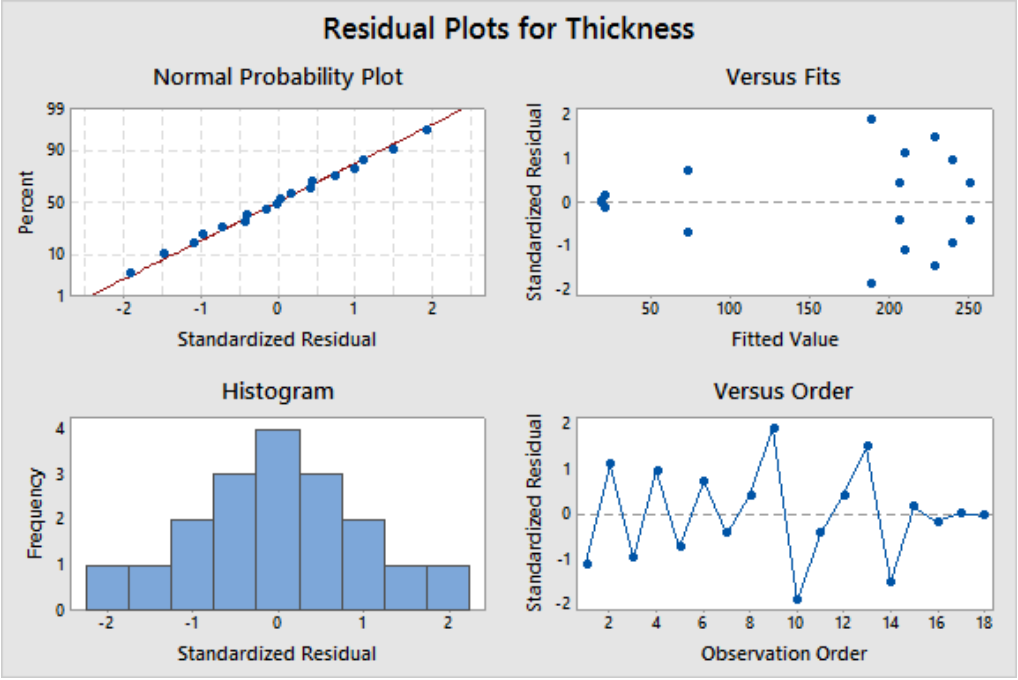

Figure A.6. Residual plots for the thickness data original general linear model.

Analysis of Variance

Continuing with the ANOVA analysis, the second General Lineal Model used Thickness as the response versus Volume and Flow Rate. The full Minitab results are in the Original Data and Minitab 17 Outputs sections following the Conclusion. In this case there were no error messages from Minitab, which means that all factors and interactions were available to be plotted. The first run of this General Lineal Model shows that there are no significant factors; however the R^2 value for model regression is very low at 57.10% thus requiring the model to be refined. After removing two obvious outlier data points Minitab produced five additional outliers, resulting in a total of seven removed points. For this analysis the R^2 value is 94.50%, which is considered a very high value for experiments.

Analysis of Variance

Source	DF	Adj SS	Adj MS	F-Value	P-Value
Volume	2	66201	33100	29.51	0.001
Flow Rate	2	15671	7835	6.99	0.027
Error	6	6730	1122		
Lack-of-Fit	2	2116	1058	0.92	0.470
Pure Error	4	4615	1154		
Total	10	122432			

Model Summary

S	R-sq	R-sq(adj)	R-sq(pred)
33.4915	94.50%	90.84%	81.02%

Coefficients

Term	Coef	SE Coef	T-Value	P-Value	VIF
Constant	159.6	11.0	14.53	0.000	
Volume					
40	61.5	18.9	3.25	0.017	1.97
50	49.7	16.5	3.01	0.024	2.17
Flow Rate					
0.3	55.5	14.9	3.73	0.010	1.58
0.4	-38.3	17.1	-2.24	0.067	1.81

Minitab could not estimate the Volume*Flow Rate interaction term for this model. However, Volume and Flow Rate factors are both significant. The values of 40 and 50 ml are significant as are showed in Analysis ANOVA table and for Flow Rate only 0.3 mL/min is significant.

Despite this refined model having a very high R^2 value, it was decided that the analysis did not properly represent the data set since almost half of the data needed to be removed. Therefore, for further conclusions the refined model with only two chosen outliers was used.

This ANOVA result is below, indicating only the Volume factor as significant based on the p-value. The R^2 value of 72.94% was determined to be acceptable for experimentation.

Analysis of Variance

Source	DF	Adj SS	Adj MS	F-Value	P-Value
Volume	2	82289	41145	4.97	0.045
Flow Rate	2	33365	16683	2.02	0.203
Volume*Flow Rate	4	44884	11221	1.36	0.339
Error	7	57917	8274		
Total	15	214006			

Model Summary

S	R-sq	R-sq(adj)	R-sq(pred)
90.9606	72.94%	42.01%	*

Coefficients

Term	Coef	SE Coef	T-Value	P-Value	VIF
Constant	182.0	23.7	7.68	0.000	
Volume					
40	10.7	34.3	0.31	0.763	1.55
50	82.7	34.3	2.41	0.047	1.55
Flow Rate					
0.3	47.8	32.0	1.50	0.178	1.35
0.4	16.7	34.3	0.49	0.641	1.42
Volume*Flow Rate					
40 0.3	-30.8	45.8	-0.67	0.523	1.76
40 0.4	29.9	47.4	0.63	0.548	1.88
50 0.3	-61.4	45.8	-1.34	0.222	2.02
50 0.4	55.7	52.0	1.07	0.320	2.27

From the p-values produced in this version of the refined model, the Volume of 50 mL appears to be the only significant setting to determine thickness.

Effects Analysis for Optimum Values

Using the refined model with only the two obvious outliers removed yields the main effects plot in Figure A.7. By selecting the highest response points on the plot, the optimum values to obtain the highest thickness are 50 mL and 0.3 mL/min.

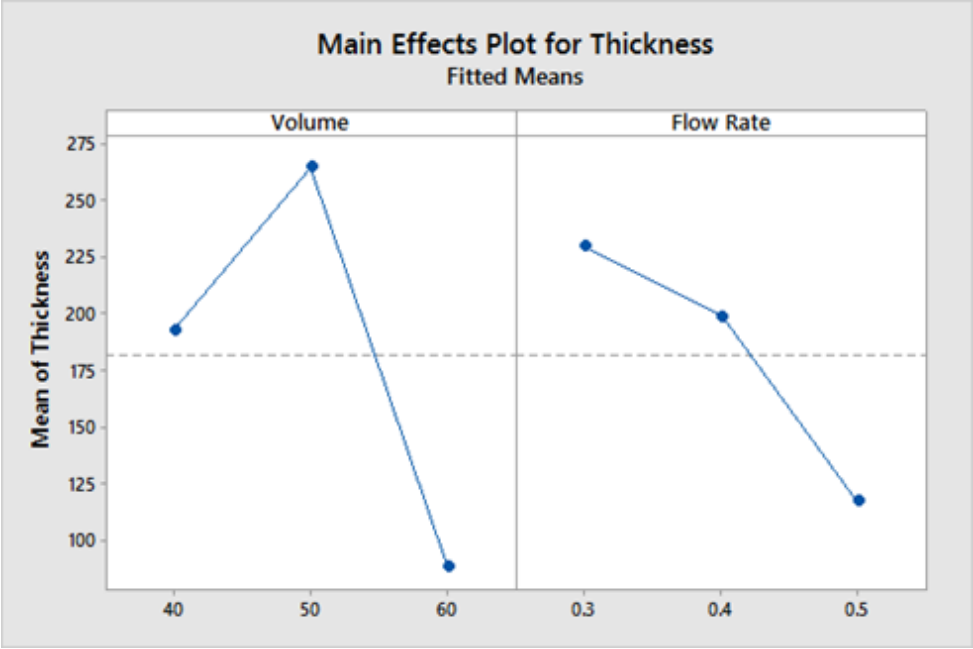

Figure A.7. Main effects plot for the Thickness response with respect to the Volume and Flow Rate factors.

Conclusions

To sum up, the goal of the project was to produce the high quality carbon nanotube nanoforest which depends on the Volume and Flow Rate factors. Based on analyzing the data in Minitab as a general linear model, ANOVA analysis shows that the Flow Rate factor is most significant to obtain a good uniform growth area and the Volume factor is most significant to the thickness of CNNs. Taking the best values from the analyses of both Area and Thickness responses, it can be determined that the best settings to have the balance of large uniform growth area and thickness are 50 mL precursor volume and 0.3 or 0.4 mL/min precursor volumetric flow rate. Since the flow rate is not significant in determining the growth thickness, 0.4 mL/min will be selected for future experiments to reduce the time of growth periods. The flow rate of 0.4 mL/min also produced the best uniform area response. Therefore, the ideal settings are 50 mL and 0.4 mL/min.

Original Data

Table A1: Measured Data

Volumetric Flow Rate / **Precursor Volume**	**0.3 mL/min**		**0.4 mL/min**		**0.5 mL/min**	
	Mass (g)	***Area (in^2)***	***Mass (g)***	***Area (in^2)***	***Mass (g)***	***Area (in^2)***
40 mL	0.3634	7.25	0.3166	11	0.0464	7
	0.6994	9	0.7060	9.5	0.3432	8
50 mL	0.5802	8	0.6382	10.5	0.3781	9.75
	0.6716	9	0.0698	12	0.6343	8
60 mL	0.8387	8.75	0.1015	6.75	0.0509	8
	0.2171	11	0.0128	12	0.0485	7

Table A2: Calculated Thickness Values in Micrometers

Volumetric Flow Rate / **Precursor Volume**	**0.3 mL/min**	**0.4 mL/min**	**0.5 mL/min**
40 mL	123.8	163.6	15.3
	295.7	315.1	129.0
50 mL	218.1	337.0	173.2
	284.0	39.3	238.4
60 mL	344.8	32.2	19.1
	112.2	7.2	15.9

Table A3: Data Used for Minitab Analysis

Volumetric Flow Rate / **Precursor Volume**	**0.3 mL/min**		**0.4 mL/min**		**0.5 mL/min**	
	Thickness (um)	***Area (in^2)***	***Thickness (um)***	***Area (in^2)***	***Thickness (um)***	***Area (in^2)***
40 mL	123.8	7.25	163.6	11	15.3	7
	295.7	9	315.1	9.5	129.0	8
50 mL	218.1	8	337.0	10.5	173.2	9.75
	284.0	9	39.3	12	238.4	8
60 mL	344.8	8.75	32.2	6.75	19.1	8
	112.2	11	7.2	12	15.9	7

Minitab 17 Outputs

Original Area Model

General Linear Model: Area versus Volume, Flow Rate

```
Method

Factor coding  (-1, 0, +1)


Factor Information

Factor     Type   Levels  Values
Volume     Fixed       3  40, 50, 60
Flow Rate  Fixed       3  0.3, 0.4, 0.5


Analysis of Variance

Source               DF  Adj SS  Adj MS  F-Value  P-Value
  Volume              2   2.632   1.316     0.51    0.616
  Flow Rate           2  16.674   8.337     3.24    0.087
  Volume*Flow Rate    4   6.806   1.701     0.66    0.634
Error                 9  23.125   2.569
Total                17  49.236


Model Summary

      S    R-sq  R-sq(adj)  R-sq(pred)
1.60295  53.03%     11.28%       0.00%


Coefficients

Term                 Coef  SE Coef  T-Value  P-Value   VIF
Constant            9.028    0.378    23.89    0.000
Volume
  40               -0.403    0.534    -0.75    0.470  1.33
  50                0.514    0.534     0.96    0.361  1.33
Flow Rate
  0.3              -0.194    0.534    -0.36    0.724  1.33
  0.4               1.264    0.534     2.37    0.042  1.33
Volume*Flow Rate
  40 0.3           -0.306    0.756    -0.40    0.695  1.78
  40 0.4            0.361    0.756     0.48    0.644  1.78
  50 0.3           -0.847    0.756    -1.12    0.291  1.78
  50 0.4            0.444    0.756     0.59    0.571  1.78


Regression Equation

Area = 9.028 - 0.403 Volume_40 + 0.514 Volume_50 - 0.111 Volume_60 -
 0.194 Flow Rate_0.3
       + 1.264 Flow Rate_0.4 - 1.069 Flow Rate_0.5 - 0.306 Volume*Flow Rate_40 0.3
       + 0.361 Volume*Flow Rate_40 0.4 - 0.056 Volume*Flow Rate_40 0.5
       - 0.847 Volume*Flow Rate_50 0.3 + 0.444 Volume*Flow Rate_50 0.4
       + 0.403 Volume*Flow Rate_50 0.5 + 1.153 Volume*Flow Rate_60 0.3
       - 0.806 Volume*Flow Rate_60 0.4 - 0.347 Volume*Flow Rate_60 0.5
```

```
Fits and Diagnostics for Unusual Observations

Obs   Area    Fit  Resid  Std Resid
 15   6.75  9.38  -2.63      -2.32  R
 16  12.00  9.38   2.62       2.32  R

R  Large residual
```

Area Refined Model after removing two unusual observations

General Linear Model: Area versus Volume, Flow Rate

```
The following terms cannot be estimated and were removed:
   Volume*Flow Rate


Method

Factor coding  (-1, 0, +1)


Factor Information

 Factor      Type   Levels  Values
Volume       Fixed       3  40, 50, 60
Flow Rate  Fixed    3  0.3, 0.4, 0.5


Analysis of Variance

 Source      DF  Adj SS  Adj MS  F-Value  P-Value
  Volume       2   2.671  1.3357     1.68    0.235
  Flow Rate  2  17.107  8.5534   10.75    0.003
Error        10   7.956  0.7956
  Lack-of-Fit   3   1.143  0.3811     0.39    0.763
  Pure Error    7   6.813  0.9732
Total        14  30.850


Model Summary

       S    R-sq  R-sq(adj)  R-sq(pred)
0.891949  74.21%     63.90%      42.54%


Coefficients
```

```
 Term         Coef  SE Coef  T-Value  P-Value   VIF
Constant     8.995    0.252      35.68  0.000
Volume
  40        -0.370   0.328  -1.13    0.286  1.14
  50         0.547   0.328  1.67     0.127  1.14
Flow Rate
  0.3       -0.630   0.328  -1.92    0.084  1.48
  0.4        1.667   0.364  4.58     0.001  1.62

 Regression Equation
Area = 8.995 - 0.370 Volume_40 + 0.547 Volume_50 - 0.177 Volume_60 - 0.630 Flow
Rate_0.3 + 1.667 Flow Rate_0.4 - 1.036 Flow Rate_0.5
```

Original Thickness Model

General Linear Model: Thickness versus Volume, Flow Rate

```
Method

Factor coding  (-1, 0, +1)


Factor Information

Factor     Type   Levels  Values
Volume     Fixed    3  40, 50, 60
Flow Rate  Fixed    3  0.3, 0.4, 0.5


Analysis of Variance

Source              DF  Adj SS  Adj MS  F-Value  P-Value
  Volume             2   49886   24943  2.07    0.183
  Flow Rate          2   52613   26306  2.18    0.169
  Volume*Flow Rate   4   42190   10548  0.87    0.516
Error                9  108693   12077
Total               17  253383


Model Summary

       S      R-sq  R-sq(adj)  R-sq(pred)
109.896  57.10%     18.97%       0.00%


Coefficients
```

```
Term                Coef  SE Coef  T-Value  P-Value   VIF
Constant           159.1    25.9   6.14    0.000
Volume
  40                14.6   36.6     0.40 0.699  1.33
  50                55.9   36.6     1.53 0.161  1.33
Flow Rate
  0.3               70.7   36.6     1.93    0.086  1.33
  0.4              -10.0   36.6    -0.27 0.790  1.33
Volume*Flow Rate
  40 0.3            -34.7  51.8    -0.67 0.520  1.78
  40 0.4             75.6  51.8     1.46 0.178  1.78
  50 0.3            -34.6  51.8    -0.67 0.521  1.78
  50 0.4            -16.8  51.8    -0.32 0.753  1.78


Regression Equation

Thickness = 159.1 + 14.6 Volume_40 + 55.9 Volume_50 - 70.5 Volume_60 + 70.7 Flow
Rate_0.3
            - 10.0 Flow Rate_0.4 - 60.6 Flow Rate_0.5 - 34.7 Volume*Flow Rate_40 0.3
            + 75.6 Volume*Flow Rate_40 0.4 - 41.0 Volume*Flow Rate_40 0.5
            - 34.6 Volume*Flow Rate_50 0.3 - 16.8 Volume*Flow Rate_50 0.4
            + 51.4 Volume*Flow Rate_50 0.5 + 69.3 Volume*Flow Rate_60 0.3
            - 58.8 Volume*Flow Rate_60 0.4 - 10.4 Volume*Flow Rate_60 0.5
```

Refined model after removing two known outliers

General Linear Model: Thickness versus Volume, Flow Rate

```
Method

Factor coding  (-1, 0, +1)


Factor Information

Factor     Type   Levels  Values
Volume     Fixed       3  40, 50, 60
Flow Rate  Fixed       3  0.3, 0.4, 0.5


Analysis of Variance

Source              DF  Adj SS  Adj MS  F-Value  P-Value
  Volume             2   82289   41145     4.97    0.045
  Flow Rate          2   33365   16683     2.02    0.203
  Volume*Flow Rate   4   44884   11221     1.36    0.339
Error                7   57917    8274
Total               15  214006


Model Summary
```

```
      S    R-sq  R-sq(adj)  R-sq(pred)
90.9606  72.94%     42.01%           *


Coefficients

Term                Coef  SE Coef  T-Value  P-Value   VIF
Constant           182.0     23.7     7.68    0.000
Volume
  40                10.7     34.3     0.31    0.763  1.55
  50                82.7     34.3     2.41    0.047  1.55
Flow Rate
  0.3               47.8     32.0     1.50    0.178  1.35
  0.4               16.7     34.3     0.49    0.641  1.42
Volume*Flow Rate
  40 0.3           -30.8     45.8    -0.67    0.523  1.76
  40 0.4            29.9     47.4     0.63    0.548  1.88
  50 0.3           -61.4     45.8    -1.34    0.222  2.02
  50 0.4            55.7     52.0     1.07    0.320  2.27


Regression Equation

Thickness = 182.0 + 10.7 Volume_40 + 82.7 Volume_50 - 93.4 Volume_60
+ 47.8 Flow Rate_0.3
            + 16.7 Flow Rate_0.4 - 64.5 Flow Rate_0.5 - 30.8 Volume*Flow Rate_40 0.3
            + 29.9 Volume*Flow Rate_40 0.4 + 0.8 Volume*Flow Rate_40 0.5
            - 61.4 Volume*Flow Rate_50 0.3 + 55.7 Volume*Flow Rate_50 0.4
            + 5.7 Volume*Flow Rate_50 0.5 + 92.1 Volume*Flow Rate_60 0.3
            - 85.6 Volume*Flow Rate_60 0.4 - 6.5 Volume*Flow Rate_60 0.5


Fits and Diagnostics for Unusual Observations

                                Std
Obs  Thickness    Fit  Resid  Resid
  5      129.0  129.0    0.0      *  X
  8      337.0  337.0    0.0      *  X

X  Unusual X
```

Removing two known outliers and five determined by Minitab, for a total of 7 points

General Linear Model: Thickness versus Volume, Flow Rate

```
The following terms cannot be estimated and were removed:
   Volume*Flow Rate


Method

Factor coding  (-1, 0, +1)


Factor Information
```

Factor	Type	Levels	Values
Volume	Fixed	3	40, 50, 60
Flow Rate	Fixed	3	0.3, 0.4, 0.5

Analysis of Variance

Source	DF	Adj SS	Adj MS	F-Value	P-Value
Volume	2	66201	33100	29.51	0.001
Flow Rate	2	15671	7835	6.99	0.027
Error	6	6730	1122		
Lack-of-Fit	2	2116	1058	0.92	0.470
Pure Error	4	4615	1154		
Total	10	122432			

Model Summary

S	R-sq	R-sq(adj)	R-sq(pred)
33.4915	94.50%	90.84%	81.02%

Coefficients

Term	Coef	SE Coef	T-Value	P-Value	VIF
Constant	159.6	11.0	14.53	0.000	
Volume					
40	61.5	18.9	3.25	0.017	1.97
50	49.7	16.5	3.01	0.024	2.17
Flow Rate					
0.3	55.5	14.9	3.73	0.010	1.58
0.4	-38.3	17.1	-2.24	0.067	1.81

Regression Equation

Thickness = 159.6 + 61.5 Volume_40 + 49.7 Volume_50 - 111.2 Volume_60 + 55.5 Flow Rate_0.3
- 38.3 Flow Rate_0.4 - 17.2 Flow Rate_0.5

Appendix B: CNN Process Purities Table

Chemical	Brand	Purity	Details
Xylenes	Sigma Aldrich	9.5%	GC Purity (sum of isomeres) ≥ 98.50 %A Xylene isomers plus Ethylbenzene GC Identified Peak ≤ 25.0 % Ethylbenzene Water (by Karl Fischer) ≤ 0.05 % Residue on Evaporation ≤ 0.002 % Substances Darkened (by H2SO4) Pass Sulfur Compounds (as S) ≤ 0.003%
Ferrocene, 98%	Sigma Aldrich	97.5%	No info on remaining 2%
Argon (AR300)	Airgas Hawaii	99.998%	Remaining 0.002% Oxygen & H_2O
Hydrogen (H330)	Airgas Hawaii	99.99%	Remaining 0.01% Oxygen & H_2O
Turco Alumiprep 33		---	Hazardous Components: Phosphoric Acid 10-30% 2-Butoxyethanol 10-30% Surfactant 1-5% Potassium Phosphate 1-5% Hydrogen Fluoride 0.1-1%
Superflex Red High Temp RTV	LOCTITE	---	(Silicone Adhesive Sealant) Hazardous Components: Distillates (petroleum), hydrotreated middle 5-10% Silicon dioxide 5-10% Silicon Resin 1-5% Diiron trioxide 1-5% Substituted Silane 1-5% Acetic acid 0.1-1% Substituted silane 0.1-1%

Appendix C: Metal Analysis of CNN GDL Samples by ICP-OES

FROM: Chuck Fraley
TO: Keith Bethune/VACNT Working Group
DATE: Oct. 31, 2015
REF: Metals Analysis of VACNT Samples by ICP-OES

Samples:
Three (3) separate samples of carbon nanotubes were obtained in plastic ziplock bags. The two smaller samples, 21.7 mg and 47 mg, were combined for one analysis. The remaining sample, 74.5 mg, was analyzed separately.

Sample Description	Sample Mass	Analysis Sample ID [Mass]
Leftover pieces from GDL tested in fuel cell, bag 1	21.7 mg	Sample 1 [68.7 mg]
Leftover pieces from GDL tested in fuel cell, bag 2	47 mg	
Alternate sample provided by Kathryn, bag 3	74.5 mg	Sample 2 [74.5 mg]

Sample Leaching/Preparation:

1. Each sample was placed in a PTFE microwave digestion tube along with 10 ml of trace metal grade HNO3, along with a blank.
2. The tubes were sealed and heated in a CEM MARSXpress microwave for 60 minutes at 90C.
3. Samples were allowed to cool overnight, then vented, resealed, and heated again to 110C for 60 mins.
4. Samples were again cooled overnight, 1.0 ml of 30% H_2O_2 were added to each sample, resealed, and heated to 110C for 60 mins.
5. The next day, the samples were transferred to 50 ml centrifuge tubes to try and separate the acid solution from the remaining CNT material.
    a. This was not effective.
6. The samples were allowed to sit overnight to allow them to settle on their own, and as much of the cleared acid solution as possible was pipetted off from the remaining solid material and transferred to clean plastic test tubes.
7. 2 ml aliquots of each solution were diluted with 6 ml of DDW, in duplicate, and analyzed by ICPoptical emission spectrometry. The instrument used was a Varian Vista-MPX.

ICP-OES Calibration:

1. Calibration was achieved by adding 0.80 ml of a 20 ppm std to an aliquot of the reagent blank.
2. Final concentrations of detected elements are provided in ug/gram after adjusting for the variation in density of the solutions vs. the density of the calibration std.

Results:

1. Results are presented in the following tables.
2. Values in red txt/yellow highlight are most likely due to contamination.
3. Values with black txt/green highlight are considered detectable quantities by the ICP-OES operator as a distinct peak was observed.

Element	Al	Al	B	B	Ba	Ba	Ca	Ca	Cd
Wavelength [nm]	394.401	396.152	249.678	249.772	455.403	493.408	393.366	396.847	214.439
Sample 1, Run A, ug/g	-47	-25	45	45	2	3	106	106	1
Sample 1, Run B, ug/g	-42	-20	55	56	2	3	104	104	3
Sample 2, Run A, ug/g	-4	-3	21	20	1	1	72	72	1
Sample 2, Run B, ug/g	-9	-7	46	46	1	1	73	72	-1

Element	Co	Co	Co	Cr	Cr	Cu	Cu	Fe	Fe
Wavelength [nm]	228.615	230.786	238.892	267.716	284.984	324.754	327.395	234.350	238.204
Sample 1, Run A, ug/g	36	38	38	7	6	-3	-1	9336	9458
Sample 1, Run B, ug/g	32	43	40	6	6	-1	3	9326	9436
Sample 2, Run A, ug/g	-5	0	1	26	21	3	4	6500	6579
Sample 2, Run B, ug/g	0	-2	-2	24	22	1	6	6526	6637

-

Element	K	Mg	Mg	Mn	Mn	Mo	Mo	Na	Na
Wavelength [nm]	766.491	279.553	280.270	257.610	293.931	281.615	284.824	588.995	589.592
Sample 1, Run A, ug/g	3885	-19	-19	3	4	-6	-5	310	353
Sample 1, Run B, ug/g	3878	-19	-19	4	6	-1	0	-58	-78
Sample 2, Run A, ug/g	12968	-18	-17	0	2	-8	1	-36	-73
Sample 2, Run B, ug/g	13004	-17	-17	0	0	-7	10	-32	-75

Element	Ni	Ni	P	P	Pb	Pb	Sr	Sr	Ti
Wavelength [nm]	227.021	231.604	213.618	214.914	220.353	283.305	407.771	421.552	334.941
Sample 1, Run A, ug/g	-6	-3	17077	20383	24	50	0	0	-2
Sample 1, Run B, ug/g	-4	-4	17177	20585	44	89	0	0	-1
Sample 2, Run A, ug/g	16	0	62618	75051	15	-44	0	0	-1
Sample 2, Run B, ug/g	-5	-7	63495	75325	1	62	0	0	0

Element	Ti	V	V	Zn	Zn				
Wavelength [nm]	336.122	268.796	292.401	206.200	213.857				
Sample 1, Run A, ug/g	0	-4	-2	-9	4				
Sample 1, Run B, ug/g	0	-4	0	-1	2				
Sample 2, Run A, ug/g	0	-3	-2	3	2				
Sample 2, Run B, ug/g	-1	-6	0	1	4				

Appendix D: Metal Analysis of Pure CNN Samples by ICP-OES

Element	Al	B	Ba	Ca	Cd	Co	Cr	Cu	Fe	K
Det. Limits	0.014	0.016	0.001	0.0004	0.020	0.020	0.020	0.020	0.020	0.050
CNT Sol'n.	0.043	0.154	<0.001	2.82	<0.020	<0.020	<0.020	<0.020	<0.020	6.33
RSD	0.299	0.017		0.0087						0.018
Metals Analysis Peaks			✔	✔		✔	✔		✔	✔

Element	Mg	Mn	Mo	Na	Ni	P	Pb	Sr	Ti	V	Zn
Det. Limits	0.010	0.006	0.020	0.013	0.070	0.50	0.300	0.0003	0.007	0.020	0.015
CNT Sol'n.	0.619	<0.006	0.022	70.9	<0.070	12.35	<0.30	0.0077	<0.007	<0.020	<0.015
RSD	0.012		0.512	0.025		0.013		0.019			
Metals Analysis Peaks		✔				✔	✔				

Appendix E: Polarization & Power Density Curves with Data Checks

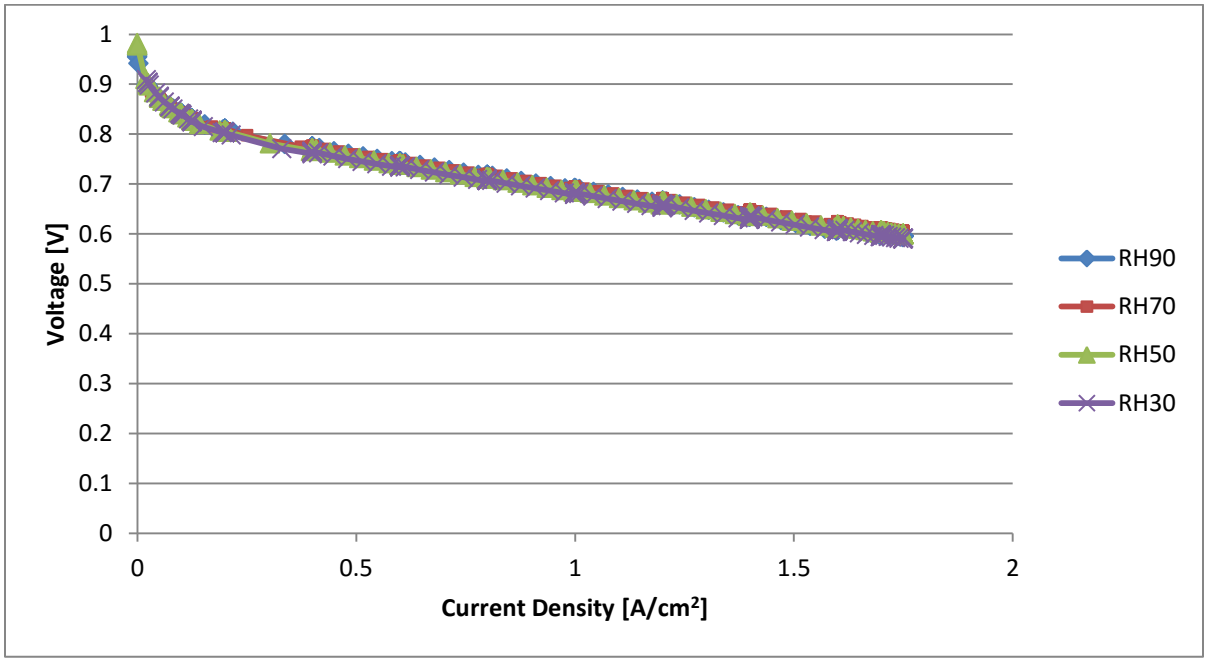

Figure E.1. Polarization curve at various RH levels for the Sigracet SGL25BC baseline GDL with O_2 at the cathode.

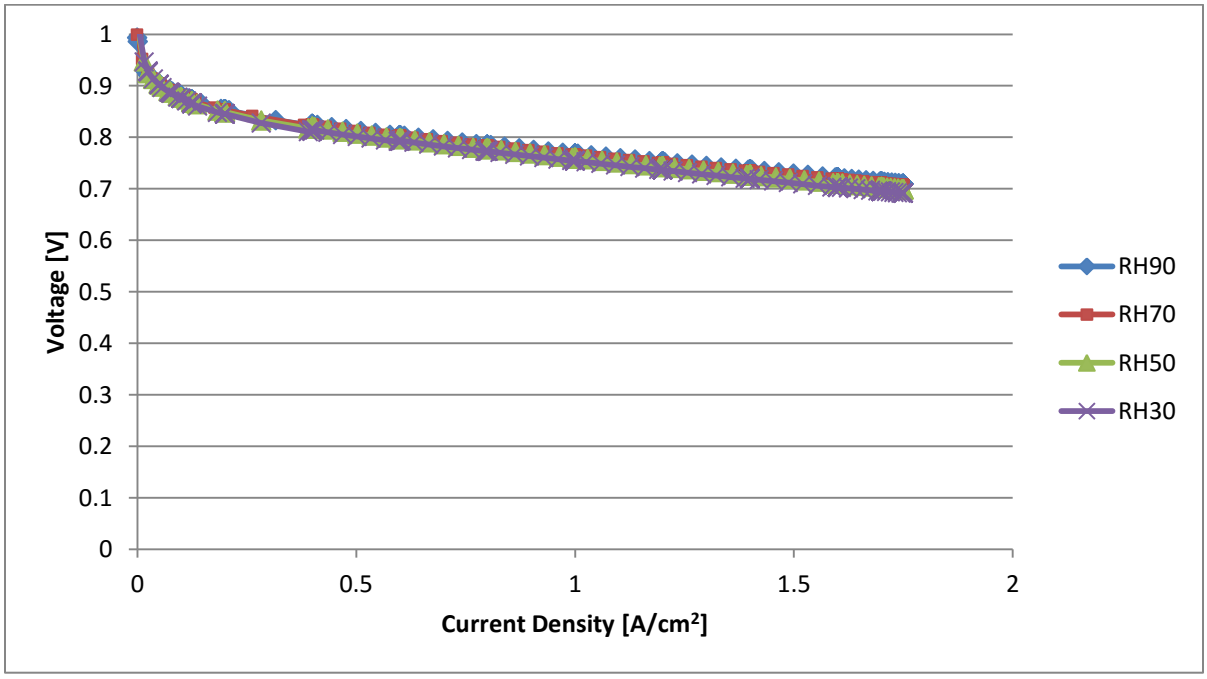

Figure E.2. Polarization curve at various RH levels for the Sigracet SGL25BC baseline GDL with air at the cathode of the cell.

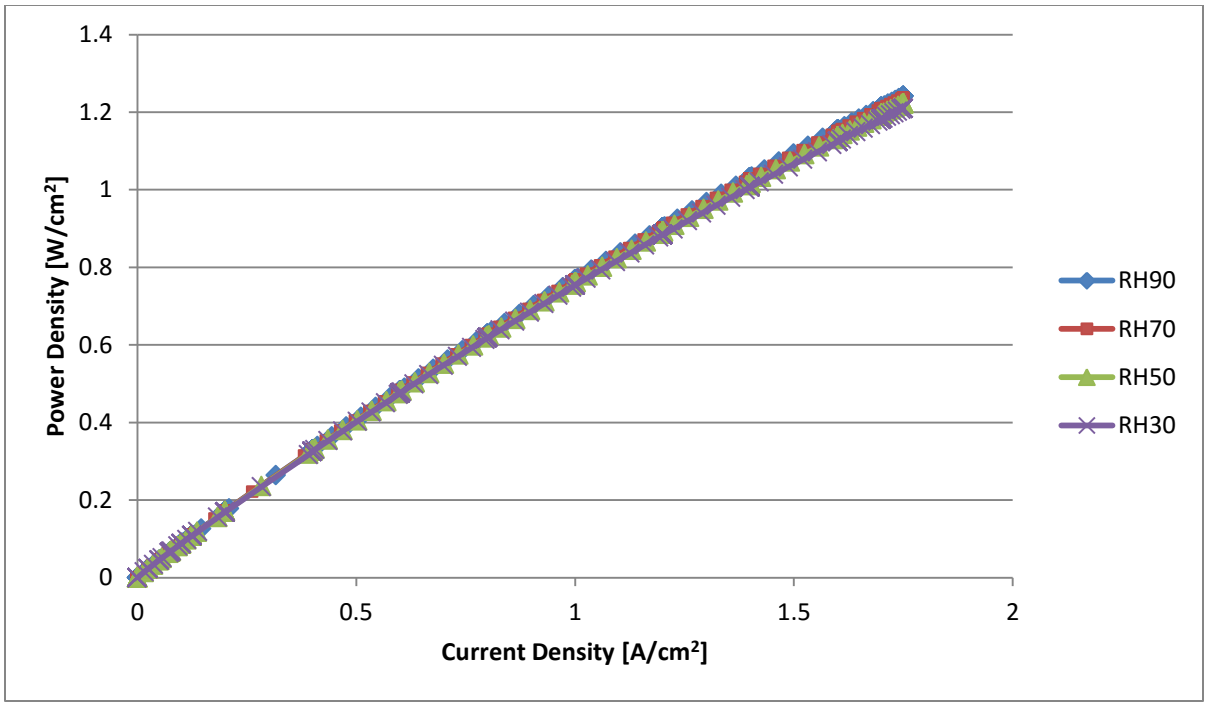

Figure E.3. Power density curves at various humidity levels for the baseline SGL25BC operating with O_2.

Looking at the baseline polarization graph in Figure E.1 with oxygen gas as the reactant on the cathode side, it exhibits the expected behavior of standard cell operation. The slope in the ohmic region of Figure E.1 is less steep than the slope in Figure E.2 corresponding to the lack of mass transport in the cell operating with pure oxygen. Due to the slight effects of mass transport with the use of air, the slopes of the curves in Figure E.2 are larger. Again focusing on the oxygen curves, the slope of this linear region should correspond to the measured HFR due to the lack of mass transport effects. The average negative slope in the ohmic region after multiplying by 50 cm^2 is 85.8 mV/A or 85.8 mΩ which is an acceptable 9% error from the averaged measured HFR. This verifies that the cell was operating properly for this test. The power curves in Figure E.3 also show the cell with the baseline GDL reaching a peak power density of approximately 1.25 W/cm^2.

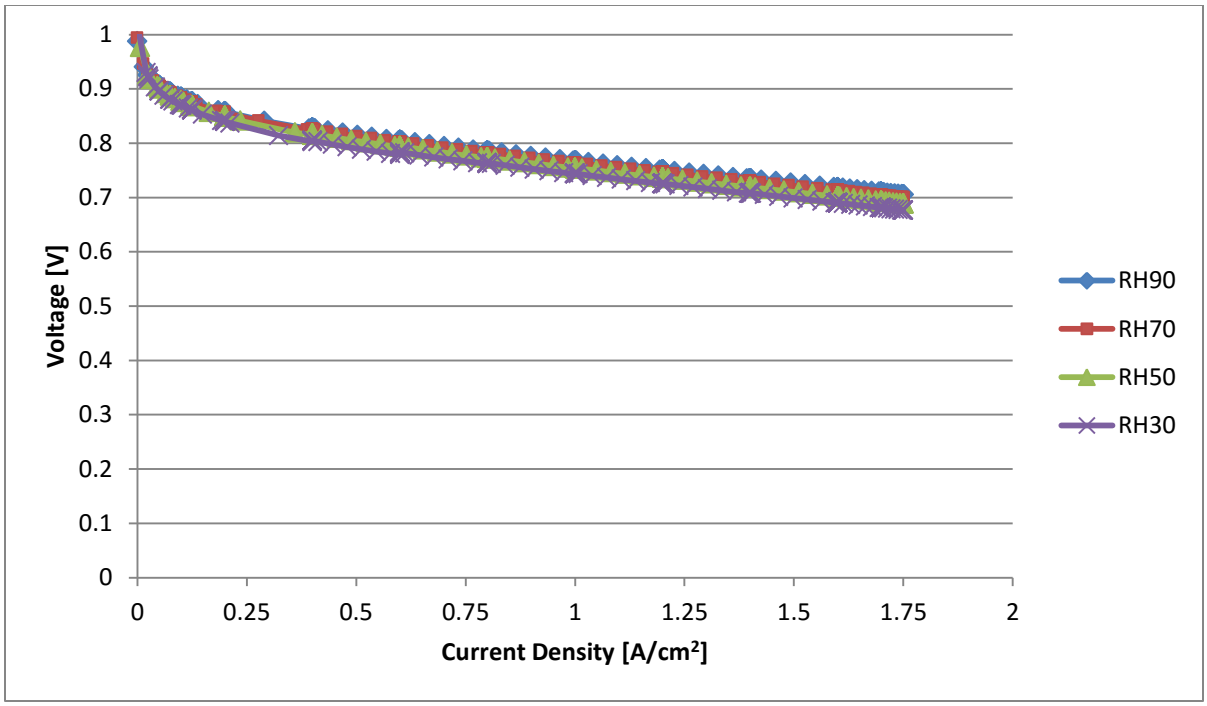

Figure E.4. Polarization curve at various RH levels for the CNN CP GDL with O_2 at the cathode of the cell.

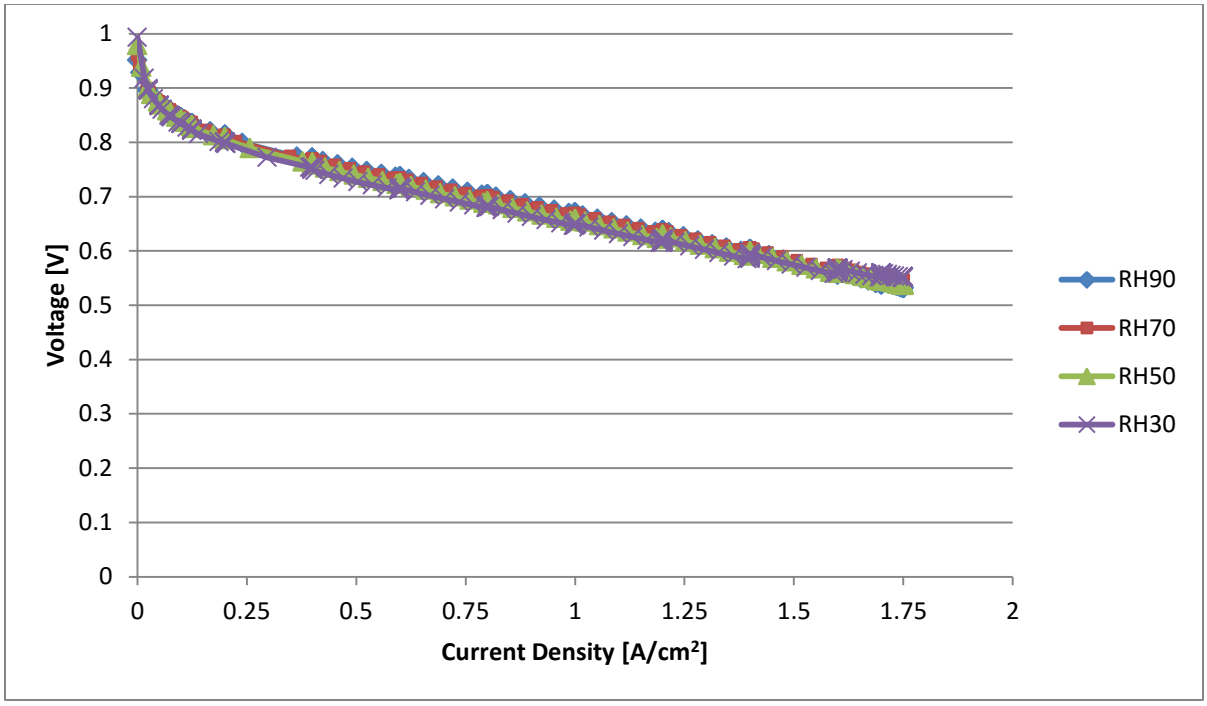

Figure E.5. Polarization curve at various RH levels for the CNN CP GDL with air at the cathode of the cell.

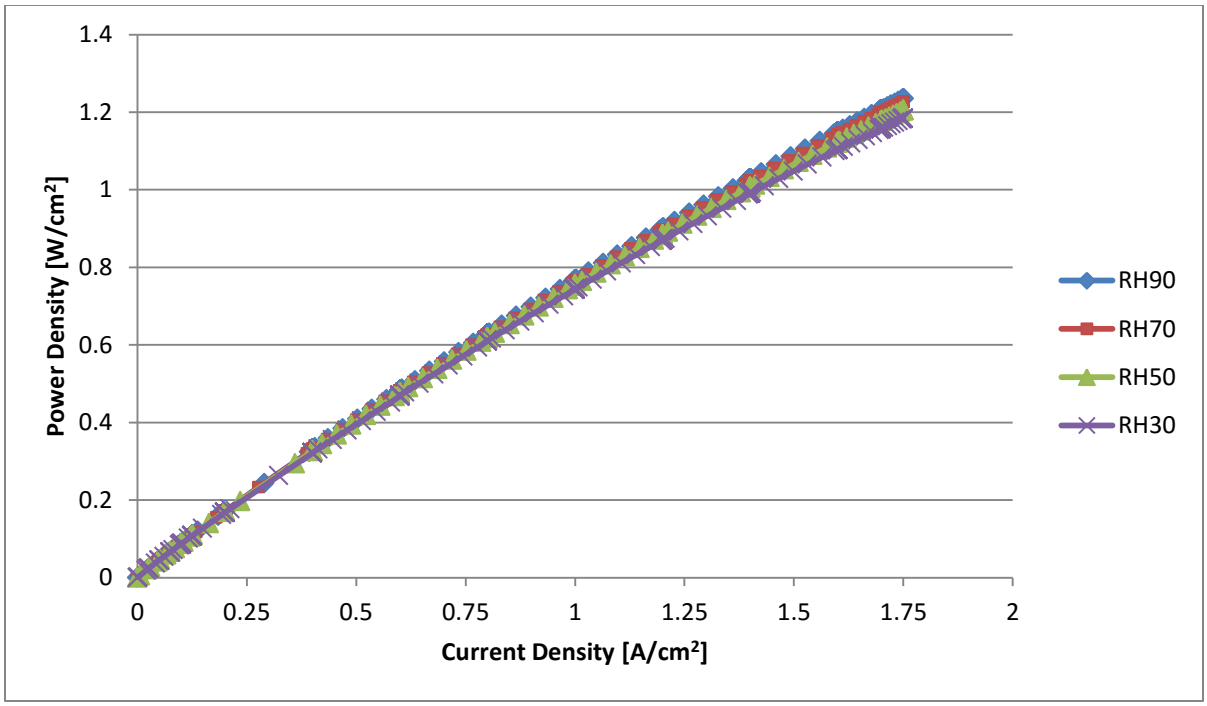

Figure E.6.Power density curves at various humidity levels for the CNN CP GDL operating with O_2.

Upon inspection of the curves produced from using the CNN CP GDL in Figures E.4 and E.5, the results look similar to that of the baseline GDL. The average negative slope was 89.7 mΩ which is 16% off from the measured HFR; therefore, the cell was not affected by mass transport as expected with the use of oxygen. However, when comparing the oxygen and air curves, the polarization curves in Figure E.5 with the use of air clearly have a steeper slope than those for oxygen. This extra voltage drop, or increased resistance, may be due to the presence of CNN. However, since the oxygen curves' average slope appropriately corresponds to the Toray TGP-H-030 CP resistance and there is no evidence of significant flooding, the CNN may not be at fault. Figure E.6 shows the power density curves for CNN CP. The peak power density of the CNN CP GDL operating with air is 1.25 W/cm^2, again very similar to the baseline. The closeness of each curve or the similar performance despite RH adjustments is an attractive feature for a potentially marketable GDL as GDLs are expected to behave consistently across a range of operating conditions.

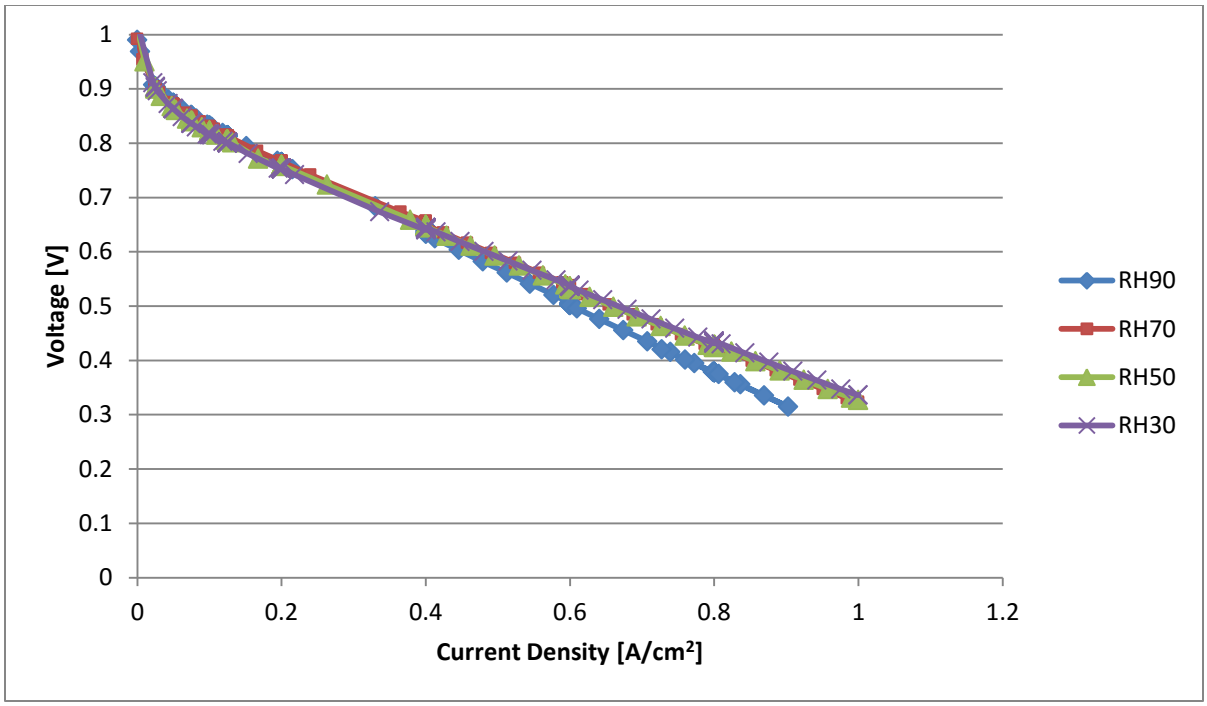

Figure E.7. Polarization curve at various RH levels for the CNN SiC GDL with O_2 at the cathode of the cell.

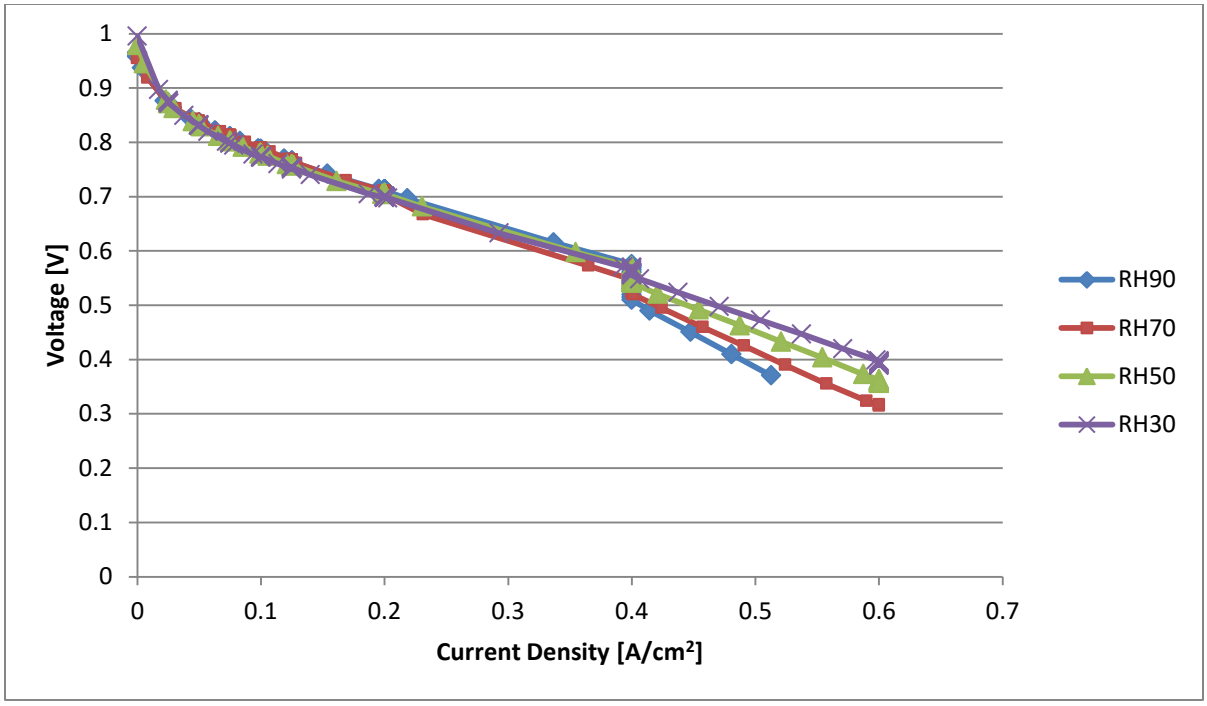

Figure E.8. Polarization curve at various RH levels for the CNN SiC GDL with air at the cathode of the cell.

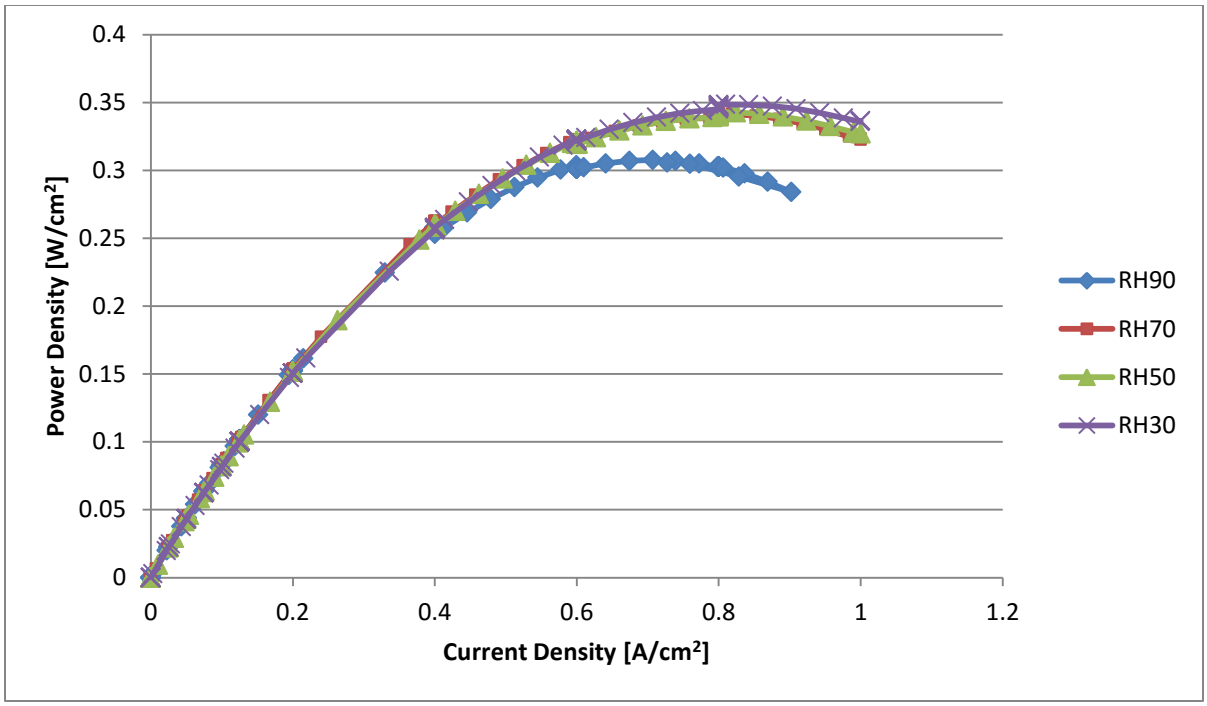

Figure E.9. Power density curves at various humidity levels for the CNN SiC GDL operating with O_2.

Figures E.7 through E.9 are the results from operating the test cell with the CNN SiC GDL. The steep slope in the ohmic region may suggest that significant mass transport effects came into play during the cell's testing cycles. However, the average negative slope was 57.1 mΩ which is 7% off from the measured HFR; therefore, the cell was not affected by mass transport but the increased resistance may be due to the ceramic's natural high resistance. Comparing the curves from the use of oxygen and the use of air, the separation between performances for each relative humidity becomes more apparent where the cell's voltage drops as RH increases. This may suggest that some flooding occurred and the liquid water could not be removed from the GDL. Similarly in the power density curves, the RH 90 setting has the worst result, noticeably lower than the other RHs which are grouped relatively closely. In addition, even at its peak power density, the CNN SiC GDL reaches only 28% of the power density achieved by the baseline GDL. This low power density coupled with the poor repeatability across the humidity range suggests that this CNN GDL with the ceramic substrate may not a good potential candidate for further research.

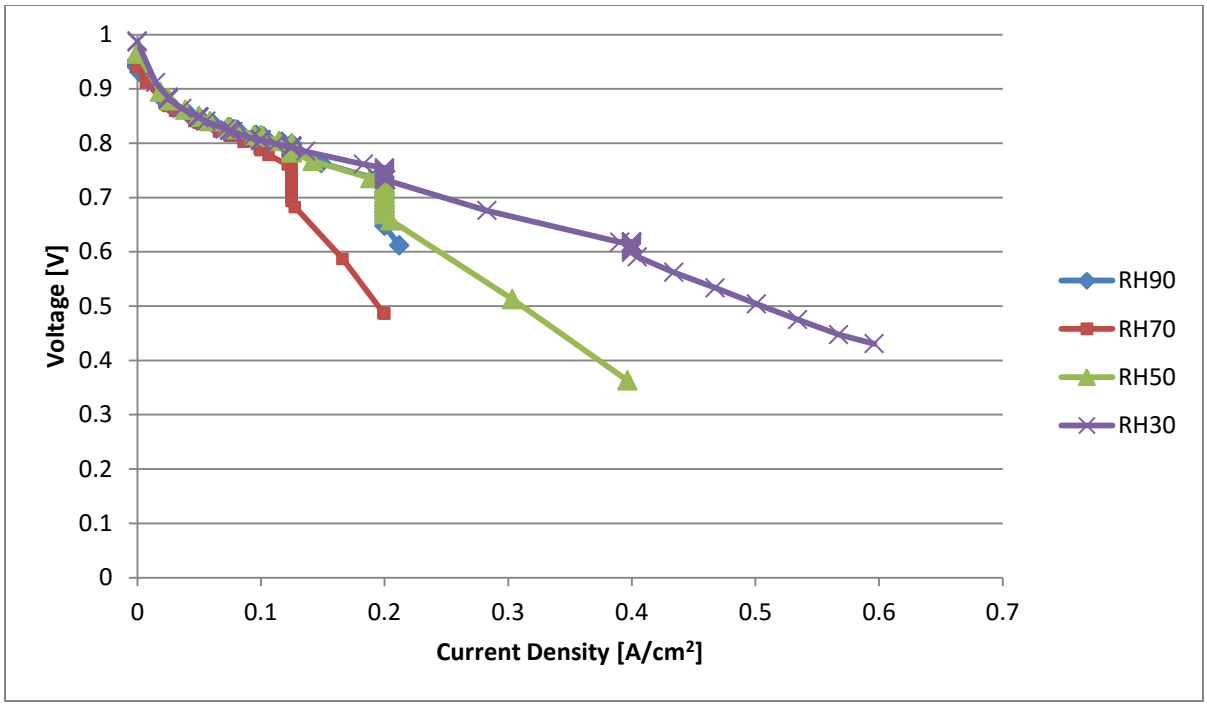

Figure E.10. Polarization curve at various RH levels for the pure CNN GDL with O_2 at the cathode of the cell.

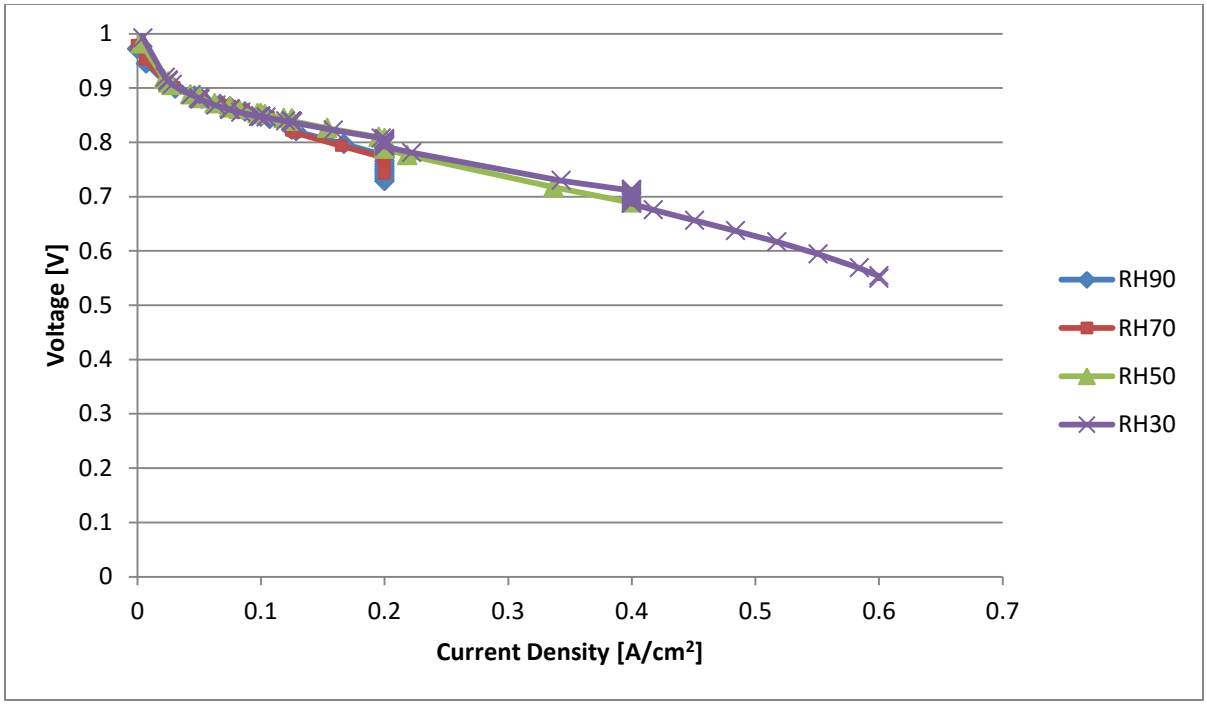

Figure E.11. Polarization curve at various RH levels for the pure CNN GDL with air at the cathode of the cell.

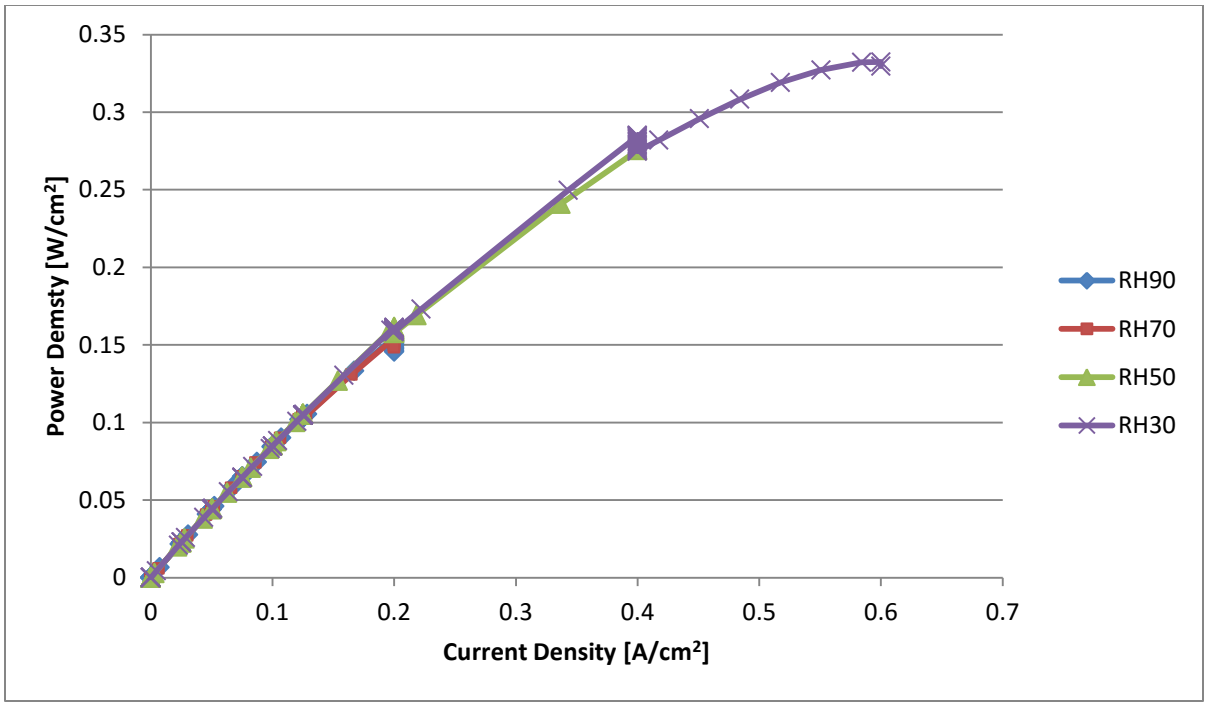

Figure E.12. Power density curves at various humidity levels for the pure CNN GDL operating with O_2.

Figures E.10 through E.12 are the results from operating the test cell with the pure CNN GDL. The test for the fuel cell with the pure CNN GDL did not reach the same intended current steps as the prior tests. This may be due to flooding and the fuel cell test station's diagnostics indicating poor performance as the curves for RH70 and RH90 are considerably shorter than that of RH30. Despite CNN being conductive, the peak power density reached approximately the same value as the SiC GDL which should have been a far less conductive material.

The following four graphs in Figures E.13 through E.16 show zoomed in views of the linear, ohmic region of the polarization curves produced with oxygen. These curves and the associated trend line equations were used to determine each GDLs voltage loss due to mass transfer and the effective mass transfer resistance for RH90 and RH30.

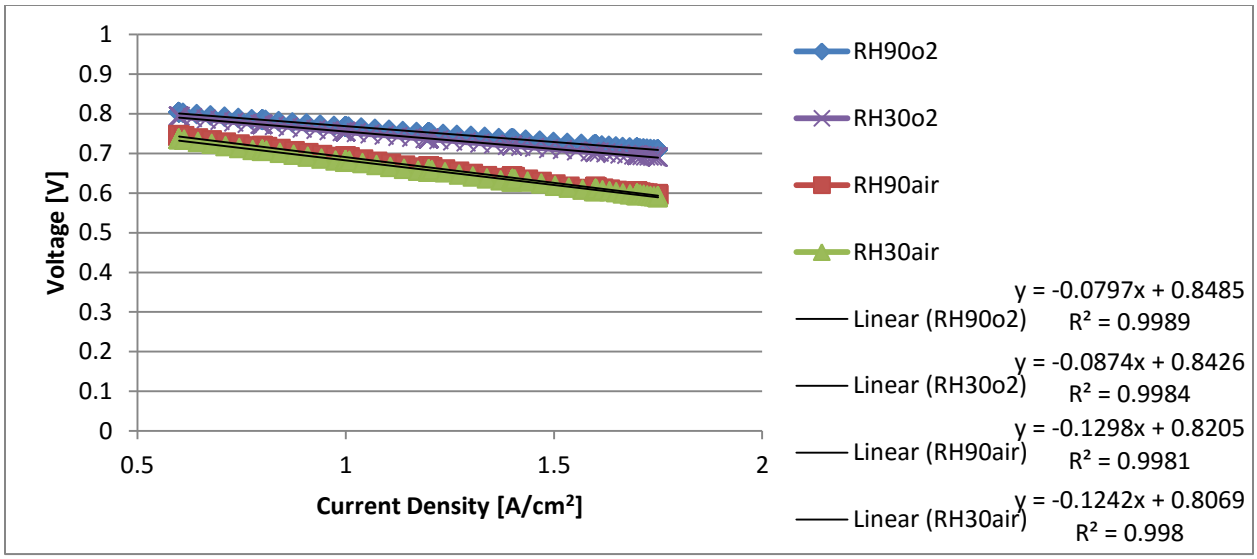

Figure E.13. Zoomed in view of the last section of the polarization curve for the baseline GDL operating with O_2 including linear trend lines and equations.

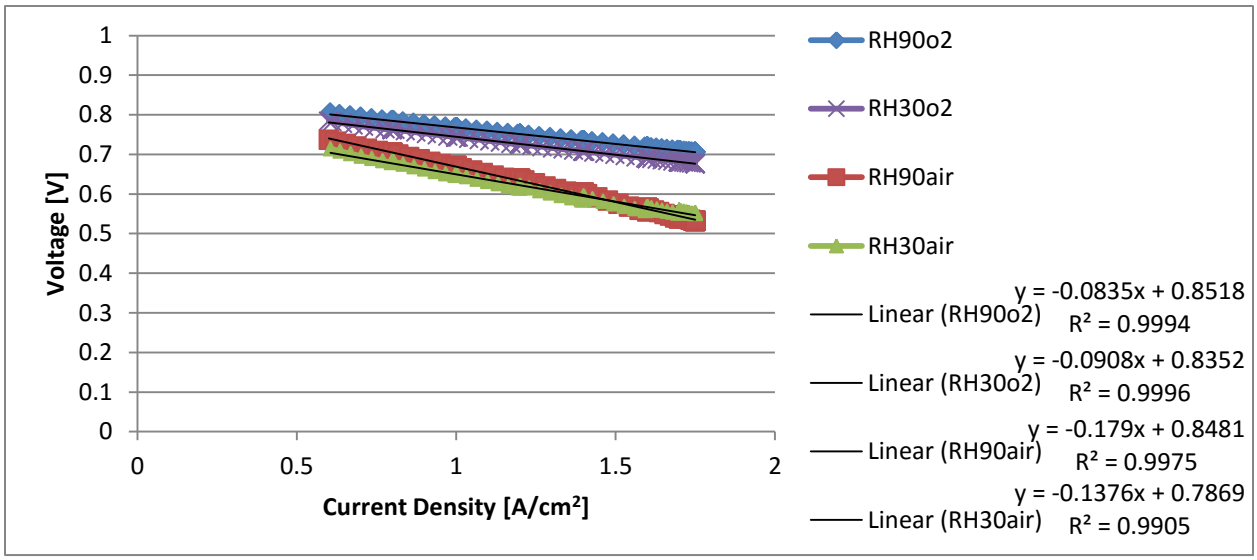

Figure E.14. Zoomed in view of the last section of the polarization curve for the CP GDL operating with O_2 including linear trend lines and equations.

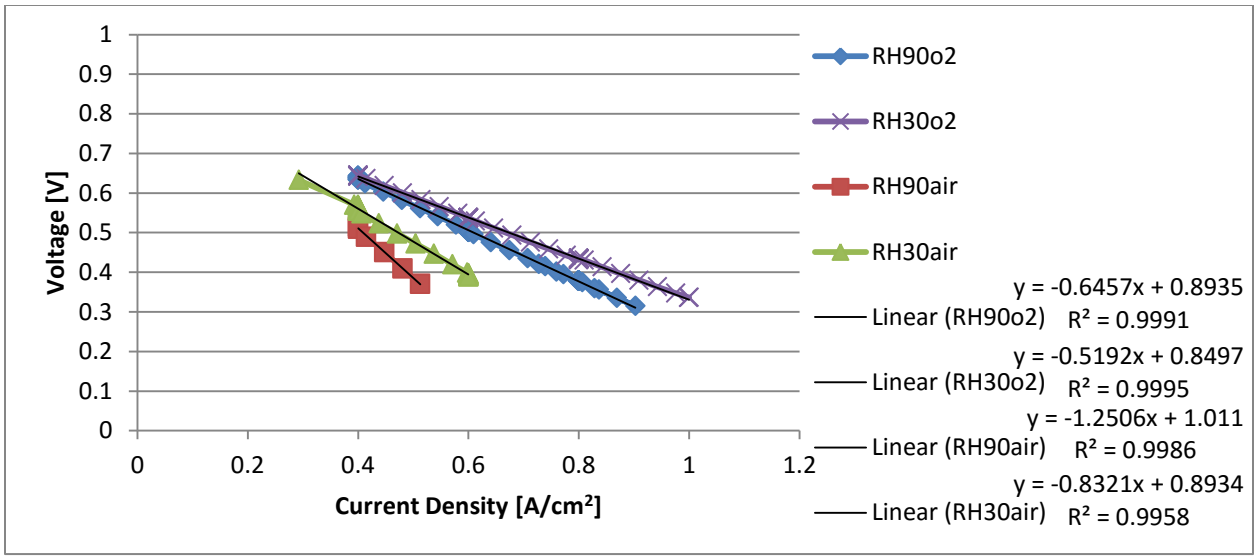

Figure E.15. Zoomed in view of the last section of the polarization curve for the SiC GDL operating with O_2 including linear trend lines and equations.

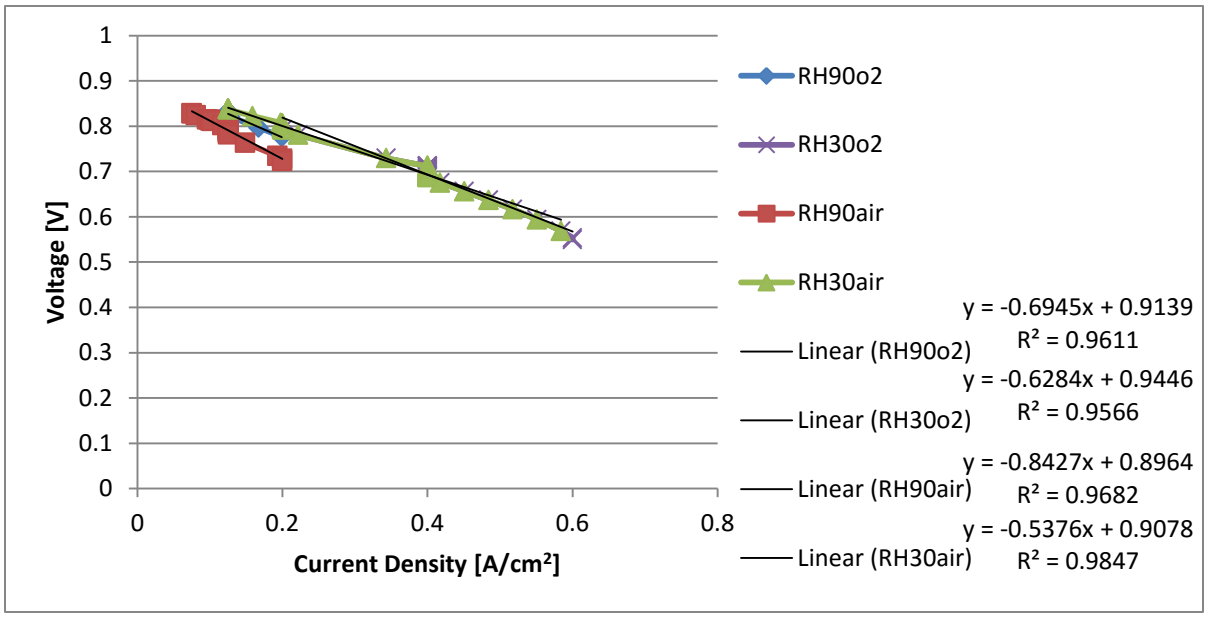

Figure E.16. Zoomed in view of the last section of the polarization curve for the pure CNN GDL operating with O_2 including linear trend lines and equations.

References

1. Whittingham, M. Stanley, Thomas Zawodzinski, and Robert F. Savinell. "Introduction: Batteries and Fuel Cells." Chem. Rev. Chemical Reviews 104.10 (2004): 4243-244. Print.
2. Service, R. F. "FUEL CELLS: Shrinking Fuel Cells Promise Power in Your Pocket." Science 296.5571 (2002): 1222-224
3. Kannan, Arunachala M., Vinod P. Veedu, Lakshmi Munukutla, and Mehrdad N. Ghasemi-Nejhad. "Nanostructured Gas Diffusion and Catalyst Layers for Proton Exchange Membrane Fuel Cells." Electrochemical and Solid-State Letters Electrochem. Solid-State Lett. 10.3 (2007): B47-B50.
4. Kannan, A.m., L. Cindrella, and L. Munukutla. "Functionally Graded Nano-porous Gas Diffusion Layer for Proton Exchange Membrane Fuel Cells under Low Relative Humidity Conditions." Electrochimica Acta 53.5 (2008): 2416-422.
5. Wan, Zhongmin, Huawei Chang, Shuiming Shu, Yongxiang Wang, and Haolin Tang. "A Review on Cold Start of Proton Exchange Membrane Fuel Cells." Energies 7.5 (2014): 3179-203. Web.
6. Park, Gu-Gon, et al. "Adoption of Nano-materials for the Micro-layer in Gas Diffusion Layers of PEMFCs." Journal of Power Sources 163.1 (2006): 113-18.
7. Dicks, Andrew L. "The Role of Carbon in Fuel Cells." Journal of Power Sources 156.2 (2006): 128.
8. Chen-Yang, Y.w., T.f. Hung, J. Huang, and F.l. Yang. "Novel Single-layer Gas Diffusion Layer Based on PTFE/carbon Black Composite for Proton Exchange Membrane Fuel Cell." Journal of Power Sources 173.1 (2007): 183-88.

9. Williams, Mike. "Scientists Refine Formula for Nanotube Types." Phys.org, n.d. Web. 10 Oct. 2014. <http://phys.org/news/2014-09-scientists-refine-formula-nanotube.html>.
10. "What Is a Carbon Nanotube?" Carbon Nanotubes. Nanocyl, n.d. Web. 10 Oct. 2014. <http://www.nanocyl.com/jp/CNT-Expertise-Centre/Carbon-Nanotubes>.
11. Zawodzinski, Thomas A., et al. "Water Uptake by and Transport Through Nafion® 117 Membranes." J. Electrochem. Soc. Journal of The Electrochemical Society 140.4 (1993): 1041. Print.
12. Büchi, Felix N., and Supramaniam Srinivasan. "Operating Proton Exchange Membrane Fuel Cells Without External Humidification of the Reactant Gases." J. Electrochem. Soc. Journal of The Electrochemical Society 144.8 (1997): 2767.
13. Zawodzinski, Thomas A. "A Comparative Study of Water Uptake By and Transport Through Ionomeric Fuel Cell Membranes." J. Electrochem. Soc. Journal of The Electrochemical Society 140.7 (1993): 1981.
14. Bernardi, Dawn M. "Water-Balance Calculations for Solid-Polymer-Electrolyte Fuel Cells." J. Electrochem. Soc. Journal of The Electrochemical Society 137.11 (1990): 3344.
15. Sridhar, P., Ramkumar Perumal, N. Rajalakshmi, M. Raja, and K.s Dhathathreyan. "Humidification Studies on Polymer Electrolyte Membrane Fuel Cell." Journal of Power Sources 101.1 (2001): 72-78.
16. Ren, Xiaoming, and Shimshon Gottesfeld. "Electro-osmotic Drag of Water in Poly(perfluorosulfonic Acid) Membranes." J. Electrochem. Soc. Journal of The Electrochemical Society 148.1 (2001): A87.

17. Chiang, M-S, and H-S Chu. "Effects of Temperature and Humidification Levels on the Performance of a Proton Exchange Membrane Fuel Cell." Proceedings of the Institution of Mechanical Engineers, Part A: Journal of Power and Energy 220.5 (2006): 435-48.
18. Wood, David L., Jung S. Yi, and Trung V. Nguyen. "Effect of Direct Liquid Water Injection and Interdigitated Flow Field on the Performance of Proton Exchange Membrane Fuel Cells." Electrochimica Acta 43.24 (1998): 3795-809.
19. Chen, Dongmei, Wei Li, and Huei Peng. "An Experimental Study and Model Validation of a Membrane Humidifier for PEM Fuel Cell Humidification Control." Journal of Power Sources 180.1 (2008): 461-67.
20. Angelo, M., Bender, G., and Bethune, K. “Calculating Operating Parameters: Main Gas Flow Rates, Contaminant Gas Flow Rates, and Dew-Points/Humidification.” Hawaii Natural Energy Institute (2009).
21. Y. Wang, C.Y. Wang, K.S. Chen, Elucidating differences between carbon paper and carbon cloth in polymer electrolyte fuel cells, Electrochim. Acta 52 (2007) 3965.
22. El-Kharouf, Ahmad, Thomas J. Mason, Dan J.l. Brett, and Bruno G. Pollet. "Ex-situ Characterisation of Gas Diffusion Layers for Proton Exchange Membrane Fuel Cells." Journal of Power Sources 218 (2012): 393-404.
23. Chen-Yang, Y.w., T.f. Hung, J. Huang, and F.l. Yang. "Novel Single-layer Gas Diffusion Layer Based on PTFE/carbon Black Composite for Proton Exchange Membrane Fuel Cell." Journal of Power Sources 173.1 (2007): 183-88.
24. Lim, Chan, and C.y. Wang. "Effects of Hydrophobic Polymer Content in GDL on Power Performance of a PEM Fuel Cell." Electrochimica Acta 49.24 (2004): 4149-156.

25. Su, Huaneng, Cordellia Sita, and Sivakumar Pasupathi. "The Effect of Gas Diffusion Layer PTFE Content on The Performance of High Temperature Proton Exchange Membrane Fuel Cell." International Journal of Electrochemical Science 11 (2016): 2919-926.
26. Stuckey, P. A., J. F. Lin, A. M. Kannan, and M. N. Ghasemi-Nejhad. "Gas Diffusion Layers for Proton Exchange Membrane Fuel Cells Using In Situ Modified Carbon Papers with Multi-walled Carbon Nanotubes Nanoforest." *Fuel Cells* 10.3 (2010): 369-74.
27. Aqel, Ahmad, Kholoud M.m. Abou El-Nour, Reda A.a. Ammar, and Abdulrahman Al-Warthan. "Carbon Nanotubes, Science and Technology Part (I) Structure, Synthesis and Characterisation." Arabian Journal of Chemistry 5.1 (2012): 1-23.
28. Mukul Kumar (2011). Carbon Nanotube Synthesis and Growth Mechanism, Carbon Nanotubes - Synthesis, Characterization, Applications, Dr. Siva Yellampalli (Ed.), ISBN: 978-953-307-497-9, InTech, DOI: 10.5772/19331. Available from: <http://www.intechopen.com/books/carbon-nanotubes-synthesis-characterization-applications/carbon-nanotube-synthesis-and-growth-mechanism>.
29. Ghasemi-Nejhad, Mehrdad N., and Vamshi M. Gudapati. Nanotape and Nanocarpet Materials. Patent WO 2011106109 A2. 1 Sept. 2011.
30. Gudapati, Vamshi, "Use of Nanoparticles and Nanotubes for the Development of High-Performance Nanoresins and Nanocomposites," PhD Dissertation, Department of Mechanical Engineering, University of Hawaii at Manoa, Honolulu, Hawaii, May 2011.
31. "Sigracet 29 BC." Fuel Cell Store. N.p., n.d. Web. <http://www.fuelcellstore.com/sigracet-29bc>.

32. A.F. Stalder, G. Kulik, D. Sage, L. Barbieri, P. Hoffmann, "A Snake-Based Approach to Accurate Determination of Both Contact Points and Contact Angles," Colloids And Surfaces A: Physicochemical And Engineering Aspects, vol. 286, no. 1-3, pp. 92-103, September 2006.

33. "Fuel Cell Hardware." FuelCell.com. ElectroChem Inc., 17 Aug. 2015. Web. 20 Apr. 2017. <http://fuelcell.com/fuel-cell-hardware/>.

34. Reshetenko, Tatyana V., Guido Bender, Keith Bethune, and Richard Rocheleau. "Systematic Study of Back Pressure and Anode Stoichiometry Effects on Spatial PEMFC Performance Distribution." Electrochimica Acta 56 (2011): 8700-710. Print.

35. "Toray Carbon Fiber Paper "TGP-H"." Fuel Cell Store. Web. <http://www.fuelcellstore.com/spec-sheets/toray-carbon-paper-data-sheet.pdf>.

36. "GDL 24 & 25 Series Gas Diffusion Layer.” Sigracet. SGL Group. Web. <http://www.fuelcellsetc.com/store/DS/SGL-GDL_24-25.pdf>.

37. “Nicalon SiC Fiber.” COI Ceramics, Inc.. Web. < http://www.coiceramics.com/pdfs/Nicalon.pdf>

38. Mathias, M. F., J. Roth, J. Fleming, and W. Lehnert. "Diffusion Media Materials and Characterisation." Handbook of Fuel Cells - Fundamentals Technology and Applications. John Wiley & Sons, Ltd, 15 Dec. 2010.

39. Martinez, Michael J., Sirivatch Shimpalee, and J. W. Van Zee. "Measurement of MacMullin Numbers for PEMFC Gas-Diffusion Media." Journal of The Electrochemical Society 156.1 (2009): B80-85.

40. Williams, Minkmas V., Eric Begg, Leonard Bonville, H. Russell Kunz, and James M. Fenton. "Characterization of Gas Diffusion Layers for PEMFC." Journal of The Electrochemical Society 151.8 (2004): A1173-1180.